

PREFERENTIAL OXIDATION OF CARBON MONOXIDE IN A THIN-FILM
CATALYTIC MICROREACTOR: ADVANTAGES AND LIMITATIONS

X. Ouyang,¹ L. Bednarova,¹ P. Ho,² R.S. Besser¹

¹New Jersey Center for Microchemical Systems
Department of Chemical, Biomedical and Materials Engineering
Stevens Institute of Technology
Castle Point on Hudson
Hoboken, NJ 07030

²Reaction Design, Inc.
6440 Lusk Boulevard, Suite D-205
San Diego, CA 92121

ABSTRACT

Silicon microreactors with thin-film wall catalyst were adopted for kinetic studies of CO preferential oxidation (PrOx). The activity of this catalyst was compared to other catalyst systems based on similar formulation. Internal and external mass transport and heat transport limitations of the microreactor were examined and comparisons were made to typical packed-bed lab reactors (m-PBR's). We found that at lower temperatures ($<220^{\circ}\text{C}$), the microreactor shows negligible mass and heat transport resistance, implying direct access to intrinsic kinetics. However, external mass transport begins to play a significant role in limiting overall reaction rates above 220°C for PrOx. A microkinetic reaction model for PrOx was used for the study of reaction pathways and the analysis of surface intermediate species which are difficult to study experimentally. Reaction mechanisms are discussed with these modeling results as a guide. Afterwards, the results of a separate, non-isothermal reactor model using the finite difference method are discussed to understand differences in performance of the microreactor and m-PBR's with respect to the CO conversion vs. temperature characteristic. As a result, we discovered that the temperature gradients in m-PBR's favor the reverse water-gas-shift (r-WGS) reaction, thus causing a much narrower range of permissible operating temperature compared to the microreactor. Accordingly, the extremely efficient heat removal of the microchannel/thin-film catalyst system eliminates temperature gradients and efficiently prevents the onset of the r-WGS reaction.

1. INTRODUCTION

Research in fuel cells has boomed in the last decade because of growing societal interest in energy-efficiency and environmental compatibility [1]. Among the various ranges of power demand, it is generally agreed that the earliest broad commercial adoption of fuel cells will be in the portable and transportation power areas [1,2]. The proton-exchange membrane fuel cell (PEMFC) is viewed as most promising for these applications due to its high power density, rapid start-up time, and low temperature operation [1,2]. An essential requirement for the PEMFC is the deep removal of CO from the H₂ stream after hydrocarbon fuel reforming and water-gas-shift reactions. This process, referred to as CO preferential oxidation (PrOx), must reduce CO from ~ 1% to below 10 ppm with minimal H₂ consumption.

Studies in PrOx reactors have generally focused on different catalyst systems [3-13] and reactor designs [3,15-17]. Pt/Al₂O₃ has been the most studied PrOx catalyst because of its high CO conversion and stability at moderate temperatures (~200 °C). With this system, Kahlich *et al.* [3] observed a maximum CO conversion at 200 °C with a selectivity of ~40%. They found that H₂ with surface oxygen can produce a hydroxyl intermediate, which enhances the catalytic activity at temperatures below 200°C. With the same catalyst system, Zafiris and Gorte [4] discovered a relationship between CO desorption and Pt particle size, i.e., the CO desorption rate rises with the decreasing Pt particle size at a given loading, which in turn influences the CO reaction rate. In order to improve the PrOx reaction activity at lower temperature (~ 100°C), Farrauto *et al.* [5,6] and Roberts *et al.* [7] explored Pt/Al₂O₃ promoted with Fe, which provides independent O₂ adsorption sites when Pt sites are dominated by adsorbed CO at

low temperatures and hence increases the CO oxidation activity. Other noble metals have also received attention. Oh and Sinkevitch [8] observed a higher selectivity of ~80% with ~100% CO conversion under non-steady state conditions with Ru/ γ -Al₂O₃ and Rh/ γ -Al₂O₃. Choudhary *et al.* [9] discovered that nano-Au catalyst with a temperature programmed reduction-oxidation pretreatment exhibited high activity and stability for CO oxidation. Metal oxide [10] and bimetallic catalysts [11] were also investigated. Preparation and pretreatment methods have been considered as another route to gain better catalytic activity by affecting material structure and particle size. Son *et al.* [12,13] developed a water pretreatment method for Pt/Al₂O₃ which resulted in a high CO conversion at low temperatures (<100 °C). The improvement was claimed to be due to the strong metal-support interaction (SMSI) between Pt and Al atoms. Serre *et al.* [14] explored the influence of pretreatment steps of Pt-CeO₂/Al₂O₃, with the discovery that after a reductive pretreatment, the Pt-CeO₂ interaction leads to a great enhancement of reactivity, which was attributed to Pt⁰-CeO₂ sites localized at the platinum-ceria interface.

Until now, most PrOx studies have been based on minimized packed-bed reactors (m-PBR's) with diameters of ~ 5 mm or larger, which, due to the large heat generation from two oxidation reactions (Equations 1 and 2), are susceptible to mass and heat transport limitations [15,16]. Therefore, practical PrOx reactor designs often adopt small catalyst particles (~ 50 μ m radius) to reduce the mass transport resistance [3,16] and multi-stage reactor systems with heat exchangers to quench the high local temperatures caused by the large heat transport resistance [17]. The drawback of adopting small catalyst particles is the increase of pressure drop while the multi-stage reactor systems increase overall system size, complexity, and above all, packaging and operation cost. Microreactors are generally accepted to

have the advantages of fast response time, ease in integration, and small footprint, which are ideal for portable power systems [18,19]. In addition, enhanced mass and heat transport properties are also widely agreed as advantages of microreactors, which are supported by the evaluation of transport properties of microreactors based on particulate and wall catalysts in various studies [20]. However, there is no literature report on transport properties of microreactors for PrOx.

Silicon microreactors were designed and fabricated with state-of-the-art micromachining techniques. Well dispersed and active Pt/Al₂O₃ catalysts were synthesized with traditional sol-gel method and then immobilized as thin films in microchannels with a novel infiltration technique. Reaction studies were carried out in a microkinetic array, with 4 reactors scanned in a rapid multiplex fashion.

Mass and heat transport properties for the microreactor with thin-film catalyst are evaluated and comparison is made to other bench-scale lab reactors. CO reaction activities of the thin-film Pt/Al₂O₃ catalyst at different temperatures are compared to other catalyst systems based on similar catalyst formulation. A reaction model based on 28 surface elementary reactions is used and reaction behavior is discussed with the simulation results. Finally, the discrepancy between the microreactor and the m-PBR on the operating temperature window associated with the reverse water-gas-shift reaction (r-WGS) is discussed with the results of a computational non-isothermal reactor model.

2. EXPERIMENTAL

2.1 Microreactors

Various materials have been explored for microreactors, e.g., stainless steel because of its robustness and good thermal conductivity, ceramic materials for high temperature application, polymers for biological compatibility and silicon due to its mature fabrication infrastructure, low cost and mass production capability. Silicon was favored in this research because of the accordance between advantages of silicon fabrication and the requirements for low-temperature fuel cell applications.

The silicon chips used in this study were fabricated with well-known micromachining processes. Photolithography and deep reactive ion etching (DRIE) by inductively coupled plasma (ICP) were the major techniques applied. Either 8 (on a 4" wafer) or 40 devices (on an 8" wafer) were formed and then sawn to gain individual chips. Anodic bonding of the silicon chip to a piece of PyrexTM glass closed the reactor, before or after catalyst incorporation in the microchannel. The finished chips have the same configuration of two inlets for the introduction of air and simulated reformat, a pre-mixer, a single channel with immobilized thin-film catalyst, a cooling channel for reaction quenching and an outlet (Figure 1). The microchannel dimensions were determined a priori through analytical modeling with a literature kinetic expression for CO oxidation [21]. All reactors discussed in this paper have dimensions of 500 μm (width) x 470 μm (depth) x 4.5 cm (length). Detailed information on the microreactor fabrication has been published elsewhere [18].

2.2 Catalysts and Reactants

The thin-film wall catalyst was adopted to minimize the undesirable pressure drop of m-PBR's, since this requires extra energy for continuous fluid passage [22], which is especially undesired in portable power applications. Platinum supported on alumina was synthesized using a sol-gel technique [23,24]. The alumina support was prepared from aluminum isopropoxide (Aldrich, 99.99+%), which was added to deionized water at 85 °C to start the hydrolysis reaction resulting in a sol. Secondly, HNO₃ was added after 45 minutes of continuous stirring. Afterwards, platinum metal was introduced by using a solution of H₂PtCl₆.xH₂O (Aldrich, 99.9+%) in 1,3-butanediol (Aldrich, 99%, anhydrous) at room temperature to yield a final platinum content in the catalyst of 2 wt%. Finally, the gel (liquid catalyst precursor) was selectively deposited in the microchannel with a novel infiltration technique [25] and followed by drying in air at 80 °C for 12 hours. Multiple layers were deposited by repeating the above procedures followed by calcination at 500°C for 2 hours. SEM (LEO 982) images of the microchannel cross section show uniform thin-film layers on each of the three walls (Figure 2), with the layer thickness ranging from ~ 2 µm to ~ 5 µm depending on the numbers of coatings. The 2 to 5 µm catalyst thickness correspond to catalyst weight of roughly 0.15 to 1.5 mg. Physisorption results showed BET surface area of ~ 400 m²/g with bimodal pore distribution in the range of 0.5 to 1.35 nm and 1.35 to 17.55 nm (Quantachrome[®] AUTOSORB-1) measurement. Pt metal particle size was determined from H₂ chemisorption (Quantachrome[®] CHEMBET-3000) and confirmed by TEM (PHILIPS[®] CM20 FEG TEM/STEM). The Pt particle sizes were found to be between 2.5 and 8.0 nm.

For reaction characterization, three reactant gases were used in this study, mixture 1 - simulated reformat (1.7% CO, 68.0% H₂, 21.0% CO₂ and N₂ as balance), mixture 2 (1.7% CO, 21.0% CO₂ and

inert) and dry air (78.1% N₂ and 21.9% O₂). All gases were supplied by AirGas East, Inc. (Paterson, New Jersey). Mixtures 1 and 2 were interchanged for different studies and further purified with an on-line filter for removal of iron carbonyl before being introduced into the flow controllers.

2.3 Microkinetic Array

A microkinetic array for fast catalyst screening and process studies was used for the reaction tests (Figure 3). Four reactors can be analyzed together with 2 gas sampling valves (GSV-1 and GSV-2) multiplexing between reactors. GSV-1 is connected with 4 effluents from the reactors and is responsible for interchange between effluents. The system has one outlet, which is connected to GSV-2. GSV-2, equipped with 2 sampling loops and constantly flushed by N₂, eliminates contamination between effluents and provides a channel to GC/MS analyzers. Each microreactor is mounted on an interface block which provides temperature control units (a thermocouple, a cartridge heater and two cooling channels) to keep the reaction zone isothermal and the pre-mixer and outlet areas cooled. Isothermal temperature control is through a PID control algorithm which measures the thermocouple and controls the cartridge heater with a solid-state relay (SSR). Preliminary thermal simulation with ANSYS[®] with inert gas flows revealed that the reaction zone is essentially isothermal (less than $\pm 2^{\circ}\text{C}$ difference) even at the highest operating temperature (300°C) with efficient cooling for the inlet and outlet areas (<200°C). In addition, the interface block provides hermeticity and continuity for the experimental system by being mechanically pressed against the microreactor with o-rings placed beneath reactor

inlet/outlet. System integrity is regularly verified with vacuum leak tests. Mass flow controllers (MFC's) are used for both air and gas mixtures 1 and 2. Pressure control is not necessary for PrOx which is conducted at atmospheric pressure, but is provided for future reaction studies that require higher pressure operation. The pressure control algorithm is also through a PID loop with pressure gauge measurement and flow control in the downstream. An online micro-GC (Varian 4900) and MS (SRS QMS-200) are shared by the array for product analysis. Process control and data acquisition are automated by a LabVIEW® program.

2.4 Reaction Characterization and Analytical Methods

Reactions were carried out in the thin-film coated microchannel, after combining air and the mixture (1 or 2) in the pre-mixer. Atmospheric pressure is maintained downstream of the microreactor with negligible pressure drop (below 0.5 psi) in all flow configurations. Fresh catalyst in the reactors was first reduced with pure H₂ in the microkinetic array at 450°C for 4 hours before reaction. Unless specifically noted, the total flow rate after the pre-mixer was 5.5 Ncm³/min (Mixture 1 or 2: 5.0 Ncm³/min, Air: 0.5 Ncm³/min) and reaction temperature was ramped to 100°C, 120°C, 140°C, ..., 300°C, with 45~60 minutes at each temperature. Initial concentrations of reactant species were determined at ambient temperature before each experiment for the calculation of $n_{CO(in)}$ and hence CO conversion (Equation 4). The screening rate (with GSV-1) for each reactor in the array was determined by the time needed for each GC sample (pumping time, elution time, integration time, etc.), which was

ca. 90s and resulted in a screening rate of ~ 6 minutes/cycle in the 4-reactor array.

Three columns (1 CP-PoraPLOT Q fused silica PLOT, and 2 CP-Molsieve 5A PLOT) with 3 identical thermal conductivity detectors (TCD) equip the Micro-GC. Helium is used as the carrier gas for the PPQ column and one of the Molsieve columns; argon is used as the carrier gas for the other Molsieve column. Separation of CO_2 and H_2O is in the PPQ column while the Molsieve columns identify H_2 , O_2 , N_2 , CH_4 and CO in the mixture. The CO detection sensitivity of TCD is 1 ppm. The GC is used mainly for quantitative product analysis and the MS for qualitative analysis and real-time reaction behavior monitoring with a response time of less than 1 second.

Because of the large concentration of CO_2 in the feed and the corresponding error in the quantification of small changes in the CO_2 concentration during experiments, CO conversion is calculated on the CO consumption (Δn_{CO}), as indicated in Equation 4. Selectivity is defined as the ratio of oxygen consumption for the CO oxidation over total oxygen consumption, as can be calculated from the oxygen mass balance in Equation 5. The process parameter, λ (Equation 6), specifies the molar ratio of O_2 to CO , and has a value of 1.0 for stoichiometric reactant ratio.

Minimized packed-bed reactors (m-PBR's) are used to make comparisons to the microreactor in the discussion of reaction results. The m-PBR's are conventional tubular lab reactors for the acquisition of kinetic data, within which mass and heat transport limitations are minimized. The parameters of the m-PBR are taken from the literature, with the reactor inner diameter of 4 mm or larger and catalyst particle diameter of $\sim 100 \mu\text{m}$ [15,21]. As in the microchannel reactors, the inner surfaces are considered

isothermal as the thin walls are assumed to be in good thermal contact with the high thermal mass heating units [26].

2.5 Microkinetic Reaction Simulation with CHEMKIN[®]

The CHEMKIN[®] software [27], an integrated software package for modeling complex chemical kinetic processes, was used to understand the intrinsic reaction mechanism and to provide insight into the processes occurring in the reactor. The microreactor was primarily treated as a plug-flow reactor, because this model is computationally tractable, and thus well-suited to developing and testing chemistry models. This decision was validated by plug-flow and boundary-layer flow simulations that gave identical results for the same conditions. In addition, our mass transport studies based on experimental data showed negligible mass gradients below 240°C (Section 3.2.1) and the microkinetic simulations mainly focused on reaction temperatures between 100°C to 200°C. Some of this work was reported previously [28].

A reaction mechanism describing the detailed gas phase and surface chemical kinetics was constructed by extracting the relevant reactions from previously published work [29] and altering the rate parameters for the oxygen adsorption reaction in order to reproduce the experimental results. As shown in Table 1, the model includes 8 adsorption reactions (reactions 1 – 8), 8 desorption reactions (reactions 9 – 16) and 12 surface reactions (reactions 17 – 28) involving 9 gas-phase species (N₂, O, O₂, CO₂, H, OH, CO, H₂, H₂O) and 8 surface species (Pt(s), O(s), H(s), OH(s), H₂O(s), C(s), CO(s), CO₂

(s). Rate constants at 100°C (373K), 180°C (453K), and 300°C (573K) for each reaction are also given in Table 1.

3. RESULTS AND DISCUSSION

3.1 Elementary Reaction Steps and Reaction Mechanism

The reaction mechanism in Table 1 successfully reproduces experimentally observed CO conversions as a function of temperature (Figure 4), and thus provides a tool for understanding the molecular-level processes occurring in this system. This section contains a general discussion of the kinetic model. Explanations suggested by the model for specific experimental observations are described in Sections 3.4 and 3.5 below.

The mechanism is composed of elementary reactions and thus contains pathways that are unimportant for a given set of conditions as well as those that are important. The CHEMKIN[®] software facilitates the analysis of reaction importance by providing information on rates of production of various species from each reaction, along with measures of the sensitivity of the solution to each reaction rate. Such an analysis resulted in the reaction network in Figure 5, which shows the 9 major forward and reverse reactions that comprise the overall reaction pathways for consumption of CO and formation of H₂O and CO₂ for the conditions of interest. The steady-state net rates in the whole reactor for these 9 reaction steps at 100°C, 180°C and 300°C are also given in the figure.

In this model, O₂ adsorption (step 2) is the rate limiting step in the sequence of surface reactions for CO₂ production (steps 2, 5, 6, and 8) before CO light-off (e.g., 100°C). The identification of O₂ adsorption as the rate limiting step at low temperatures has been substantiated experimentally in various reactor studies [3,8,11,24] but could differ with operating conditions. Among the major adsorption reactions (reactions 1 – 4) for a feed containing reactants of CO, H₂, CO₂, and O₂ without H₂O (i.e., mixture 1 and air), CO adsorption (reaction 3) has the highest sticking coefficient along with a relatively slow desorption rate. As a result, CO(s) dominates the catalyst surface, severely limiting the O₂ adsorption and consequently the CO(s) oxidation. Elevated temperatures increase the CO desorption rate, which is essential to open enough Pt sites for O₂ adsorption and the onset of CO(s) oxidation.

There are two pathways for CO₂ formation: step 4 and steps 5 and 6, as shown in Figure 5. As indicated by the higher net-rate values, the major path for CO₂(s) production is through the formation of the OH(s) species (step 5) and the subsequent oxidation of CO(s) by OH(s) (step 6), rather than the direct oxidation of CO(s) (step 4). In addition, although some hydrogen must initially be present on the surface, the H(s) species needed in this path is regenerated at steady state, as indicated by the dashed line in Figure 5. The existence of the hydroxyl species and its importance on PrOx reaction activity has been reported by others [24,30,31] and is further discussed below (Section 3.5).

At low temperatures, H₂O formation is negligible, being limited by the low H(s) and O(s) coverage. Thus, at 100°C, step 5 in Figure 5 has a much higher net rate than steps 7 and 9, plus the rate of the series of steps 5, 6, and 8 is double the rate of step 2 (O₂ adsorption). The onset of CO(s) oxidation at higher temperature sharply reduces CO(s) coverage and with the fast desorption of CO₂(s),

H(s) and O(s) concentrations and the subsequent H₂O(s) production increase.

Additionally, methane formation is not considered in the reaction mechanism since both our experiments and other reports [3,5,15] found negligible methane formation for both low and high CO conversion cases below 300°C.

3.2 Mass and Heat Transport

3.2.1 Internal and External Mass Transport Limitations

In order to provide better understanding of the transport properties for the microreactor, it is necessary to examine internal and external mass transport and heat transport limitations and to make comparisons to m-PBR's. As stated previously, the parameters of the m-PBR are taken from literature values and the inner walls for both reactors are considered isothermal in the evaluation of heat transport limitations.

Internal mass transport describes movement of reactants and products inside catalyst pores, which may affect overall reaction rates for porous catalyst systems with fast surface chemistry. Estimation of internal mass transport limitation is generally realized by the calculation of the Thiele modulus (ϕ_n) and the internal effectiveness factor (η_i), or the estimation of the Weisz-Prater (W-P) parameter (C_{wp}) [32]. While a Langmuir-Hinshelwood type reaction rate expression is used for CO oxidation under wide CO, O₂ concentrations and temperatures, a power-law rate expression is generally

accepted for CO oxidation within reasonable limits of the PrOx reaction temperatures and CO and O₂ concentrations [21]. The deduced reaction orders in both the literature [3,21] and our experiments are ~ -1 for CO and ~ 1 for O₂. The negative order in CO, coupled with some mass transport resistance can lead to peculiar behavior, namely, an internal effectiveness factor (η_i) above 1 [15,21,33]. In addition, the calculation of η_i with both reactant components requires complicated numerical calculations [15,21]. On the other hand, the evaluation of internal mass transport can be based on O₂, which has ~ 1 reaction order and therefore the widely agreed upon W-P criterion can be applied.

The W-P criterion [32,33] states that if the C_{WP} (Equation 7) is much smaller than 1, then the internal mass transfer limitation is negligible. In this equation, $-r_{O_2}''(obs)$ and $C_{O_2(s)}$ are estimated at differential flow conditions, and ρ_c is taken as the density of alumina. For the thin-film catalyst, L_c equals the catalyst thickness [33,34], which is normally ~ 5 μm . In addition, D_e is estimated with Equation 8 [35]. The parameters in Equation 8 are taken either from experimental measurement or from typical literature values for particulate catalysts prepared from the same precursors as ours and with similar procedures [15,16]. In Figure 6, C_{WP} for the thin-film catalyst is plotted at different reaction temperatures, which shows $C_{WP} \ll 1$ even at the highest operating temperature. In comparison, L_c for the m-PBR (~ 50 μm) is ~ 10 times that of the microreactor and the calculated C_{WP} for the m-PBR can be ~ 100 times that for the microreactor due to its quadratic dependence on L_c . The estimated C_{WP} of the m-PBR for temperatures above 200°C no longer satisfies the $C_{WP} \ll 1$ criterion (Figure 6). In addition, the C_{WP} and η_i for the PrOx in m-PBR estimated by Kim *et al.* [15] revealed severe internal mass transport limitations above 200°C.

External mass transport is negligible below 300°C for PrOx with m-PBR's in differential flow measurements because of their relatively small catalyst particle radii (~50 μm) and hence the small external mass transport distance for reactant gases, as reported previously [15,16]. However, it is necessary to address the possibility of external mass transport limitation for our microreactor due to its comparatively longer external mass transport distance, which is from the center of the microchannel to the wall (~250 μm). Two separate quantification methods were applied to examine the external mass transfer resistance.

The first method examines the ratio of the surface and bulk gas-phase concentration for both CO and O₂ since the external mass transfer resistance can be considered negligible if both ratios are larger than 95% [36]. For differential conditions with the microreactor, bulk reactant concentrations ($C_{CO(b)}$ and $C_{O_2(b)}$) are taken as the feed reactant concentrations. Surface CO concentration ($C_{CO(s)}$) is obtained through Equation 9. The mass transfer coefficient of CO (k_{c-CO}) in Equation 9 is first estimated with the correlations described in [37], which were developed for laminar flow in parallel-plate catalyst systems (Equations 10 – 13). Afterwards, $C_{CO(s)}$ is obtained with Equation 9 by equating W_{CO} and the surface reaction rate, $-r_{CO}''$ (obtained from the microkinetic reaction simulation) at steady state. The surface O₂ concentration ($C_{O_2(s)}$) can be calculated with the same procedures. Figure 7 plots $C_{CO(s)}/C_{CO(b)}$ and $C_{O_2(s)}/C_{O_2(b)}$ at different temperatures. Both concentration ratios decrease slowly with temperature. As seen from this figure, $C_{CO(s)}/C_{CO(b)}$ and $C_{O_2(s)}/C_{O_2(b)}$ are higher than 95% below 220°C and 240°C, respectively. Our typical PrOx operating temperature is ca. 180°C and both ratios are >98%, indicating the insignificance of external mass transport resistance. However, as temperature increases above 240°C,

this advantage diminishes.

The second test for assessing external mass transport evaluates the overall specific reaction rate (k_r) (Equation 15) at different reactant flow rates. The assessment is based on a well-known method [38] for determining the limiting step between mass transport and surface reaction in a catalytic reactor. Since the change in flow rate results in different mass transport resistance, the calculated k_r would also change significantly if mass transport is limiting the reaction. On the other hand, if the change in the calculated k_r is small and without trend, it would imply that mass transport is not rate-limiting [32,35].

An experiment was carried out for this test. A microreactor coated with 0.25 mg of catalyst was adopted. The $C_{CO(b)}$ and $C_{O_2(b)}$ was varied using different flows of air and mixture 1. A constant total flow of 5.5 Ncm³/min was maintained with a third flow of N₂. The temperature was kept at 180°C during the whole experiment. The specific reaction rates (k_r) for different reactant concentrations were then evaluated using Equations 14 and 15. All data considered was taken below 10% CO conversion in order to justify the differential form in Equation 14. The low temperature and CO conversion also imply negligible r-WGS and H₂ oxidation activity. Reaction orders in the lumped power law expression were gained previously with the microkinetic reaction model ($\alpha = -0.895$; $\beta = 0.989$). The power law form (Equation 15) was adopted since it was successfully used by others for PrOx kinetics [3,16] at temperatures below 300°C and typical CO and O₂ concentrations (0.5 ~ 2%). The ratio of k_r and the average specific reaction rate ($k_{r(e)}$) was plotted against the ratio of $C_{O_2(b)}$ and $C_{CO(b)}$ in Figure 8. The calculated variation of k_r shows no dependence on the reactant flow, which further corroborates the conclusion that external mass transport is not rate-limiting in the microchannel with the thin-film

catalyst, under typical operating conditions.

In the case of integral flow measurements, the above conclusion on internal and external mass transport limitation is still justified for positive order reactions but inaccurate for negative order reactions, e.g., CO oxidation on Pt. Due to the negative reaction order in CO, CO concentration drops and the reaction rate increases with CO conversion along the reactor length. The increase in the reaction rate then leads to the increase of C_{WP} , and a growing difference between the gas and surface CO concentration (Equation 9) and hence a reduction in the $C_{CO(s)}/C_{CO(b)}$ ratio, which eventually indicates mass transport controlled conditions. For example, at 180°C, our calculation showed a transition from surface reaction control to external mass transport control within the reactor as CO conversion reaches 60% along the reactor.

To summarize the mass transport limitations for the PrOx reactors as defined above, (1) the internal mass transport limitation is significant for the m-PBR's above 200°C and negligible for the microreactor even at 300°C; (2) with differential flow conditions, the microreactor has apparent external mass transport limitation above 240°C while the external mass transport limitation of the m-PBR's is generally considered negligible below 300°C [15,16]; (3) with integral flow conditions, mass transport becomes important with large CO conversion in both types of reactors.

3.2.2 Heat Transport Limitations

Efficient reaction heat removal reduces the temperature gradients inside the reactor and effectively prevents the high temperature reverse water-gas-shift (r-WGS) reaction for PrOx (Section 3.6). There are three domains of heat transport inside the reactor – intraparticle (within a porous catalyst particle or the catalyst layer in case of the thin-film catalyst), interphase (between the external surface of the catalyst and the fluid adjacent to it) and interparticle (between the catalyst particles and the reactor inner wall) transport [39].

Mears [39] suggested that the magnitudes of the heat transport resistances are generally in the order of interparticle > interphase > intraparticle when the thermal Biot number (Bi) is small (Equation 17) and the heat transfer resistance at the reactor wall are negligible. First, a Biot number (Equation 17) smaller than 10 implies that the interphase heat transport resistance becomes limiting before the intraparticle heat transport resistance [40]. In this calculation, d_p for the microreactor is $\sim 5 \mu\text{m}$ and d_p for the m-PBR is $\sim 100 \mu\text{m}$; the heat transfer coefficient (h) for the reactant gas is within the range of $10 \sim 100 \text{ W/m}^2\text{-K}$ [40] and the effective thermal conductivity (λ_e) is in the order of 0.1 W/m-K for the porous catalyst [16]. The calculated Biot numbers are much smaller than 10 for both reactors. Secondly, the hydraulic diameters of both reactors are much larger than the catalyst thickness or particle size (>50 times), indicating a negligible heat transfer resistance at the reactor wall [40]. In addition, because the extent of the reaction front (i.e., the reactor axial length needed for complete CO conversion) at typical PrOx reaction temperature (200°C) is much greater than the catalyst thickness or particle size (>30 times) for both the microreactor and the m-PBR, axial heat conduction is neglected in the following discussion [40,41].

Since the radial interparticle heat transport resistance is most critical for both types of reactors, calculations of the *Damköhler* numbers (D_a) in Equation 16 can provide a qualitative comparison of heat transport limitations [40,41]. If the left hand side is smaller than the right hand side, the radial temperature difference in the reactor would be less than 5% [40,41]. For the microreactor, t_{cat} is $\sim 5 \mu\text{m}$ and t_{cat} is $\sim 2.5 \text{ mm}$ for the m-PBR. CO reaction rate ($-r_{CO}$) is taken at 200°C (T_w) due to the wide availability of rate data of PrOx on Pt/Al₂O₃ at this temperature in the literature. Literature values of $-r_{CO}$ for PrOx with m-PBR's range from $0.02 \sim 0.5 \text{ mol/m}^3\text{-s}$ [3,4,15]. In comparison, $-r_{CO}$ calculated from the microreactor with Pt/Al₂O₃ catalyst is $1.43 \text{ mol/m}^3\text{-s}$ at 200°C . The activation energy and reaction heat of CO oxidation on Pt/Al₂O₃ (E_a) are $\sim 75000 \text{ J/mol}$ and 280000 J/mol [42]. The calculation results by applying the above values in Equation 16 show that the left hand side for the microreactor is orders of magnitude smaller than the right hand side while the left hand side for m-PBR's are higher than the right hand side. In conclusion, the microreactor has negligible thermal gradient while the heat transport resistance of the m-PBR is significant for PrOx because of the microreactor's extremely short t_{cat} compared to the m-PBR.

3.3 Comparison of Catalyst Activity

The activity of the Pt/Al₂O₃ thin-film catalyst was compared to other Pt/Al₂O₃ catalyst systems for CO oxidation studies reported in the literature with the calculation of turnover frequencies (*TOF*'s), using Equation 18. The comparison is summarized in Table 2 for 5 temperature regions ($\sim 100^\circ\text{C}$, 150°C ,

~200°C, ~220°C, 250°C). Certain TOF's from our work were scaled slightly using our experimentally-based lumped kinetic model (Equation 15) to compare to literature values. These values required scaling due to the variety of reformat compositions in the literature and our use of pre-mixed reformat. In addition, this kinetic model was gained with similar reaction conditions used in other research works and studies [3] showed insignificant effect on the reaction activity with these divergences in concentrations. Our experimental results showed that total pressures are 1 atm, except for Sirijaruphan *et al.* [43] and Ajmera *et al.* [16].

There are three observations from this table. (1) For each temperature region, the TOF's for CO oxidation with H₂ addition is higher than the ones without H₂. This is consistent with adsorbed hydrogen and oxygen creating a hydroxyl species and a second CO oxidation pathway, as we discussed in Section 3.1. (2) The thin-film catalyst has *TOF* similar to other catalyst systems in each temperature region for CO oxidation without H₂ addition. This similarity is not surprising since both the thin-film catalyst and other catalyst systems listed in the table are based on similar Pt/Al₂O₃ formulation. (3) For CO oxidation with the H₂ addition, the thin-film catalyst appears to have close TOF's to other catalyst systems at low temperatures (~100°C, 150°C) but greater activity at higher temperatures (~200°C, 250°C). We believe this higher *TOF* of the thin-film catalyst at high temperature is due to the superior temperature management provided by the microchannel environment, leading to better control over the side r-WGS reaction (Equation 9), which lowers the net CO conversion, as discussed in Section 3.2. In this sense, the microchannel provides greater access to intrinsic catalyst behavior than the m-PBR's.

3.4 Conversion and Selectivity

The study of conversion and selectivity showed characteristic behavior for all microreactors tested. A representation of this behavior is shown in Figure 9, which had 1.5 mg of 2 wt% Pt/Al₂O₃ catalyst (WHSV = 1500 hr⁻¹, $\lambda = 2.57$). Mildly rising slopes of CO and O₂ conversion with negligible H₂ oxidation before CO light-off (<160°C) was followed by sharp increases of CO, O₂ and H₂ conversion during CO light-off (160°C~180°C). O₂ conversion was less than half of the CO conversion before CO light-off because the O₂/CO feed ratio is more than twice the reaction stoichiometry (2.57). However, a rapid O₂ conversion followed and reached ~90% at 180°C just after CO light-off, indicating the onset of O₂ conversion with both CO and H₂. Consequently, CO₂ selectivity showed a slight increase (<160°C) followed by a sharp decrease (160°C~180°C) with the temperature rise. This behavior agrees qualitatively with other PrOx studies on Pt/Al₂O₃ [3,11,24,44].

The experimentally-observed behavior of conversion and selectivity can be understood with the help of the microkinetic reaction simulation. As discussed in Section 3.1, the catalyst active sites in the model are dominated by CO(s) before light-off. Correspondingly, the H(s) coverage is only ~0.1 despite its large gas concentration and the oxygen has only a trace of surface coverage (Figure 10). CO₂ is produced preferentially to H₂O before CO light-off (<160°C) also because of the high CO(s) coverage, which severely limits the rate of H₂ adsorption and H₂O formation, (steps 3, 7 and 9 in Figure 5). As a result, CO conversion slightly increases with no appreciable H₂ conversion below 160°C (Figure 9). However, at higher temperatures during and after light-off (>160°C), the CO(s) coverage drops steadily due to the increased CO(s) desorption rate and the onset of CO(s) oxidation, allowing a concomitant

increase of H(s) mole fraction (Figure 10). The rates of the H₂O formation steps (steps 3, 7 and 9 in Figure 5) then rise substantially and cause the decline of CO₂ selectivity from ~100% to ~40% at higher temperatures.

3.5 CO Conversion Enhancement by H₂

Several researchers [3,8] have observed an activity enhancement effect by H₂ while others [5,11,12,24,44] found similar behavior with the addition of H₂O. Among these reports, Avgouropoulos *et al.* [11] and Nibbelke *et al.* [44] excluded the WGS reaction as the enhancement mechanism due to the low WGS reaction rate on Pt/Al₂O₃. Manasilp *et al.* [24] suggested the modification of the ratio of the Pt₀ to Pt(O)_x as the mechanism without providing further evidence. Behm *et al.* [3,30], corroborated the existence of a hydroxyl species with *in-situ* diffuse reflectance infrared Fourier transform spectroscopy (DRIFTS) but did not discuss the detailed elementary reaction steps related to this enhancement. In order to study the effect and intrinsic mechanisms of H₂ on PrOx reaction with the thin-film catalyst, we carried out experiments using two mixtures, one without H₂ and a second with H₂, as described in the caption of Figure 11. Our experimental results qualitatively agree with the literature that the light-off slope shift to lower temperature with H₂ in the reactant stream at the temperatures before and during light-off.

In addition, as shown in Figure 11, the microkinetic simulations also indicate a large increase in CO conversion in the presence of hydrogen. In this case, the simulations in the absence of hydrogen

actually show considerably less conversion than is observed experimentally. However, the simulations using this reaction mechanism are very sensitive to the presence of small amounts of water. For example, for a temperature of 180°C, adding 0.1 ppm of H₂O to the starting gas mixture raises the CO conversion by a factor of 6.6 to 0.08%, while adding 1 ppm of H₂O increases the CO conversion in the simulation all the way up to 50%. Such low levels of water are likely to have been present in the experimental system, either in the gases used or adsorbed on various surfaces, but difficult to determine or control in the experimental apparatus. Thus, we have chosen to show the simulations with no hydrogen or water in the simulations in the figure, but consider the agreement between model and experiment to be good.

The experimental observations, combined with the work of Behm *et al.* are consistent with our microkinetic reaction simulations. This suggests that the addition of H₂ increases the rate of CO oxidation by facilitating the formation of surface hydroxyl species. This increase is manifested as the shift of CO light-off slope to lower temperature seen in Figure 11.

3.6 Effect of Enhanced Heat Transport

A divergence in the CO conversion behavior from literature PrOx studies was found at temperatures below and above CO light-off, as shown in Figure 12. The studies based on m-PBR's with particulate catalyst found that there existed a narrow operating temperature window for CO conversion [3,8,45], followed by the decline of both CO conversion and CO₂ selectivity with further temperature increase. In contrast, our studies with microreactors showed essentially 100% CO conversion between

180°C and 280°C while there is only a slight drop-off (< 1%) at 300°C, suggesting a much wider operating window for CO conversion. An earlier explanation of this undesired falloff of both CO conversion and CO₂ selectivity was the competition between H₂ oxidation and CO oxidation [3]. Further investigations found that the falloff is caused by the r-WGS reaction, the effect of which becomes more pronounced in the presence of temperature non-uniformities [8,21,24]. Due to the fast surface chemistry of the exothermic CO oxidation (ΔH : ~ 280000 J/mol) and H₂ oxidation (ΔH : ~ -242000 J/mol) and the comparatively low thermal conductivity of the catalyst material, reaction heat can accumulate within the packed-bed, leading to an uneven temperature distribution and higher local temperatures (hot spots) in the reactor. The endothermic r-WGS reaction (Equation 3) is activated and eventually limits the net CO conversion. According to Mear's criteria of heat transport limitations (Section 3.2.2 and Equation 16), this situation gets more severe with the increase of the heat conduction distance (t_{cat}).

Various reports have made clear the importance of thermal management of PrOx reactors. In particular, Roberts *et al.* [7] studied the r-WGS using a 62 cells/cm² monolith adiabatic reactor washcoated with 5 wt% Pt/0.5 wt% Fe/Al₂O₃. They found that full O₂ conversion in the adiabatic PrOx reactor caused the downstream temperature increase to ~ 300°C with the inlet temperature of only 170°C. This temperature increase thus resulted in a significant CO production by r-WGS. Later, Choi *et al.* [45] developed a 1D m-PBR model to evaluate overall PrOx reaction performance under various reactor heat exchange conditions (adiabatic, isothermal, etc.). They concluded that the CO net conversion drops significantly as the reactor operation changes from isothermal to adiabatic conditions.

In order to further assess the effects of heat transport limitations on PrOx reaction activity, we constructed a quasi-3D non-isothermal reactor model coupled with the reaction kinetics of all major PrOx reactions (i.e., CO oxidation, H₂ oxidation and r-WGS reactions) [46]. A finite difference method was adopted to calculate the 2D temperature distribution along both the radial and axial directions, which distinguishes the approach from previous PrOx reactor modeling efforts [45]. The quasi-3D modeling is necessary since radial effects are unimportant only for adiabatic reactor operation, while large temperature gradients can form with isothermal reactor wall conditions as discussed above. The CRESLAF model of the CHEMKIN® software has functions to carry out similar studies. However, our adoption of the 1D PLUG model and the convergence problem at high CO conversion in the CRESLAF simulation (Section 2.5) prevents its use in this study. Simulations were done for both the microreactor and m-PBR's of two different sizes (2-mm and 4-mm radii). A detailed report of this model is presented in [46]. Some representative plots are discussed in this paper.

Figures 13 and 14 show the modeling results for a 2-mm m-PBR with different isothermal wall temperatures (100°C, 120°C, 140°C, 160°C, 180°C, 220°C, 260°C, 300°C). Figure 13 shows the axial temperature distribution in the center of the reactor ($r = 0$ mm). These results agree qualitatively with the 1D modeling conducted by Choi *et al.* [45] in that the temperature first increases and then decreases along the reactor axial direction. The temperature increase is proportional to the local reaction rates of CO and H₂ oxidations. Thus, the inverse dependence of both the CO and H₂ oxidation rates on C_{CO} (large C_{CO} inhibits H₂ and O₂ adsorption and the subsequent surface reactions; also see Section 3.1) leads to higher temperature as C_{CO} decreases along the axial direction and then back to the wall

temperature after O_2 is fully converted. Figure 14 then shows the radial temperature distribution at $l = l_{Tmax}$. The temperature gradient becomes more dramatic with higher wall temperatures. As the wall temperature increases, full conversions of O_2 (with CO and H_2) take place in shorter reactor lengths. Since the total reaction heat generated by the full conversion of O_2 (with CO and H_2) is nearly constant, the shorter reactor lengths for full O_2 conversion cause a high density of accumulated heat in the region close to l_{Tmax} , leading to the dramatic high temperatures in this region.

Figure 15 plots CO conversion at different wall temperatures for both the microreactor and m-PBR's with 2-mm and 4-mm radii, which all have the same WHSV and isothermal wall temperature conditions. Figure 16 then shows the reaction rates of CO oxidation, H_2 oxidation and r-WGS reaction for these 3 reactors also at same reaction conditions, found by integrating the reaction rates in the finite difference grid. In Figure 15, the CO conversion curve for the microreactor essentially coincides with the result for ideal isothermal operation without any radial or axial temperature gradients; conversely, the light-off curves for m-PBR's shift to lower temperatures and CO conversion drops significantly at the higher wall temperatures. The low temperature curve shift can be explained by an increase in CO oxidation rate at local hot spots. With further temperature increase, however, these temperature non-uniformities in m-PBR's begin to favor the r-WGS reaction, as indicated by the increasing r-WGS reaction rate with temperature (Figure 16) and the dramatic drop of net CO conversion (Figure 15). Consequently, these phenomena are more significant for the 4-mm than the 2-mm m-PBR (Figure 16). In addition, the maximum CO conversion of the 4-mm m-PBR is only $\sim 90\%$, indicating the existence of severe hot spots even at relatively low wall temperatures. The CO conversion curves from literature

PrOx studies with m-PBR's [3,8,45] agree qualitatively with these modeling results and thus can be understood with the above arguments. Due to the lack of detailed kinetic data of other PrOx catalysts in the literature, further effort to specifically predict PrOx behavior for these PrOx reactors is impractical.

Overall, the m-PBR's has severe temperature gradients with the activation of exothermic CO and H₂ oxidation reactions, leading to significant r-WGS reaction activity. In contrast, the isothermality within the microreactor effectively removes the reaction heat and minimizes the extent of the r-WGS side reaction. The sensitivity of PrOx performance on temperature brings attention to thermal management in the design of practical reactors. The suppression of severe temperature non-uniformities is important as discovered in this study.

4. CONCLUSIONS

The Pt/Al₂O₃ thin-film catalyst coated in silicon microreactors was shown to have PrOx activity comparable to other literature catalyst systems based on similar formulation. Superior heat transport properties were found with the microreactor compared to conventional lab reactors (m-PBR's) according to the comparison of D_a numbers for both systems. The minimized heat transport resistance of the thin-film catalyst appears to efficiently suppress the r-WGS reaction which would severely compromise the overall PrOx performance. Calculations were also made to evaluate internal and external mass transport limitations of the thin-film catalyst. The internal mass transport limitation was determined to be negligible due to the small characteristic dimension of the thin-film catalyst. Differential flow

calculations show the microreactor has negligible external mass transport limitation below 220°C for PrOx. For integral flow conditions, due to the negative reaction order in CO, a transition from surface reaction control to external mass transport control takes place with growing CO conversion along the reactor length.

The combination of experimental studies and detailed chemical kinetic simulations suggests that the following reaction pathways are important in this system. Before CO light-off, the Pt surface is covered by adsorbed CO, making the adsorption of O₂ rate limiting at low temperatures. At higher temperatures, after CO light-off, O₂ begins to react with H₂, reducing CO₂ selectivity to ~ 40%. The observed enhancement of H₂ addition on CO conversion temperature dependence can be explained by a new route for CO₂ formation through the indirect CO oxidation with a OH(s) intermediate species.

Finally, we discussed the side r-WGS reaction and the operating temperature window for PrOx, which are greatly affected by the heat transport efficiencies of the reactors. The results from a non-isothermal reactor model were used to facilitate the understanding of the heat transport effect. The extremely efficient heat removal of the thin-film catalyst in the microchannel virtually eliminates any temperature gradients, which are essentially inevitable for m-PBR's. The temperature gradients in the m-PBR then favor the r-WGS reaction and a narrow operating temperature window. This study also suggests the advantage of the utility of the microreactor for accessing intrinsic reaction kinetics compared to m-PBR's.

ACKNOWLEDGEMENTS

The authors gratefully acknowledge the financial support for this project from the Defense Advanced Research Projects Agency (Grant No. N66001-03-1-8903) and New Jersey Commission of Science and Technology (NJCST). The numerous discussions on the project with Profs. Woo Y. Lee and Adeniyi Lawal are acknowledged. We would also like to thank Prof. Suphan Kovenklioglu for his stimulating discussion and suggestion, Woocheol Shin for the microreactor fabrication and Haibiao Chen for preparing and characterizing the catalyst. In addition, the authors are grateful to Profs. Götz Vesper and Dion G. Vlachos for their insightful comments.

References

1. Song C, fuel processing for low-temperature and high-temperature fuel cells challenges, and opportunities for sustainable development in the 21st century. *Catal Today*. 2002;77:17–49.
2. National Fuel Cell Research Center. The Fuel Cell Resources page. Available at: http://www.nfrcr.uci.edu/fcreources/FCexplained/FC_Types.htm. Accessed July 9, 2004.
3. Kahlich MJ, Gasteiger HA, Behm RJ. Kinetics of the selective CO oxidation in H₂-rich gas on Pt/Al₂O₃. *J Catal*. 1997;171:93–105.
4. Zafiris GS, Gorte RJ. CO oxidation on Pt/ α -Al₂O₃(0001): evidence for structure sensitivity. *J Catal*. 1993;140:418-423.
5. Korotkikh O, Farrauto R. Selective catalytic oxidation of CO in H₂: fuel cell applications. *Catal Today*. 2000;62:249-254.
6. Liu X, Korotkikh O, Farrauto R. Selective catalytic oxidation of CO in H₂: structural study of Fe oxide-promoted Pt/alumina catalyst. *Appl Catal, A*. 2002;226:293-303.
7. Roberts GW, Chin P, Sun XL, Spivey JJ. Preferential oxidation of carbon monoxide with Pt/Fe monolithic catalysts: interactions between external transport and the reverse water-gas-shift reaction. *Appl Catal, B*. 2003;46:601-611.
8. Oh SH, Sinkevitch RM. Carbon monoxide removal from hydrogen-rich fuel cell feedstreams by selective catalytic oxidation. *J Catal*. 1993;142:254-262.
9. Choudhary TV, Goodman DW. CO oxidation on supported nano-Au catalysts synthesized from a [Au₆(PPh₃)₆](BF₄)₂ complex. *J Catal*. 2002;207:247-255.
10. Teng Y, Skurai H, Ueda A, Kobayashi T. Oxidative removal of CO contained in hydrogen by using metal oxide catalysts. *Int J Hydrogen Energy*. 1999;24:355-358.
11. Avgouropoulos G, Ioannides T, Papadopoulou Ch, Batista J, Hocevar S, Matralis HK. A comparative study of Pt/ γ -Al₂O₃, Au/ α -Fe₂O₃ and CuO–CeO₂ catalysts for the selective oxidation of carbon monoxide in excess hydrogen. *Catal Today*. 2002;75:157-167.
12. Son IH, Shamasuzzoha M, Lane AM. Promotion of Pt/ γ -Al₂O₃ by new pretreatment for low-temperature preferential oxidation of CO in H₂ for PEM fuel cells. *J Catal*. 2002;210:460-465.
13. Son IH, Lane AM, Johnson DT. The study of deactivation of water pretreated Pt/ γ -Al₂O₃ for low-

- temperature selective CO oxidation in hydrogen. *J Power Sources*. 2003;124:415-419.
14. Serre C, Garin F, Belot G, Maire G. Reactivity of Pt/Al₂O₃ and Pt-CeO₂/Al₂O₃ catalysts for the oxidation of carbon monoxide by oxygen. *J Catal*. 1993;141:9-20.
 15. Kim DH, Lim MS. Kinetics of selective CO oxidation in hydrogen-rich mixtures on Pt/alumina catalysts. *Appl Catal, A*. 2002;224:27-38.
 16. Ajmera SK, Delattre C, Schmidt MA, Jensen KF. Microfabricated differential reactor for heterogeneous gas phase catalyst testing. *J Catal*. 2002;209:401-412.
 17. Lee SH, Han J, Lee KY. Development of 10-kWe preferential oxidation system for fuel cell vehicles. *J Power Sources*. 2002;109:394-402.
 18. Surangalika H, Ouyang X, Besser RS. Experimental study of hydrocarbon hydrogenation and dehydrogenation reactions in silicon microfabricated reactors of two different geometries. *Chem Eng J*. 2003;93:217-224.
 19. Besser RS, Ouyang X, Surangalika H. Hydrocarbon hydrogenation and dehydrogenation reactions in microfabricated catalytic reactors. *Chem Eng Sci*. 2003;58:19-26.
 20. Kolb G, Hessel V. Micro-structured reactors for gas phase reactions: a review. *Chem Eng J*. 2004;98:1-38.
 21. Venderbosch RH, Prins W, van Swaaij WPM. Platinum catalyzed oxidation of carbon monoxide as a model reaction in mass transfer measurement. *Chem Eng Sci*. 1998;53:3355-3366.
 22. Foumeny EA, Kulkarni A, Roshani S, Vatani A. Elucidation of pressure drop in packed-bed systems. *Appl Therm Eng*. 1996;16:195-202.
 23. Zhao S, Besser RS. Selective deposition of supported platinum catalyst for hydrogenation in a micromachined reactor. *Proceedings of the 6th International Conference on Microreaction Technology*. 2002;289-296.
 24. Manasilp A, Gulari E. Selective CO oxidation over Pt/alumina catalysts for fuel cell applications. *Appl Catal, B*. 2002;37:17-25.
 25. Chen H, Ouyang X, Bednarova L, Besser RS, Lee WY. Infiltration of sol-gel synthesized Pt/Al₂O₃ thin-film catalyst into microchannel reactor. Manuscript in Preparation. 2004.
 26. Ouyang X, Besser RS. Flexible microreactor system for chemical research at moderate temperatures. *SPIE Proceedings*. 2003;4982:297-301.

27. Kee RJ, Rupley FM, Miller JA, *et al.* *Chemkin Collection, Release 3.7.1*. San Diego, Calif: Reaction Design, Inc; 2003.
28. Ouyang X, Ho P, Chen H, *et al.* Preferential oxidation in microchannel reactors for scalable fuel processing systems. AICHE 2003 Annual Meeting Proceedings. 2003;171a.
29. Zerkle DK, Allendorf MD, Wolf M, Deutschmann O. Understanding homogeneous and heterogeneous contributions to the platinum-catalyzed partial oxidation of ethane in a short-contact-time reactor. *J Catal.* 2000;196:18-39.
30. Schubert MM, Gasteiger HA, Behm RJ. Research note: surface formates as side product in the selective CO oxidation on Pt/ γ -Al₂O₃. *J Catal.* 1997;172:256-258.
31. Mhadeshwar AB, Vlachos DG. Microkinetic modeling for water-promoted CO oxidation, water-gas shift, and preferential oxidation of CO on Pt. Submitted to *J Phys Chem B*. 2004.
32. Fogler HS. Diffusion and reaction in porous catalysts. In: *Elements of Chemical Reaction Engineering*, 3rd ed. Englewood Cliffs, NJ: Prentice Hall; 2000.
33. Herz RK. Reaction and diffusion in a porous catalyst pellet. Available at: http://courses.ucsd.edu/rherz/ceng113/notes/my_notes_pdf/rxn_diff.pdf. Accessed October 20, 2003.
34. Moulijn J, Makkee M, van Diepen A. *Chemical Process Technology*. Chicester, NY: John Wiley and Sons, Ltd; 2001.
35. Satterfield CN. *Mass Transfer in Heterogeneous Catalysis*. Cambridge, Mass: The MIT Press; 1969.
36. Reactor and Catalyst Engineering, Delft University. Mass and heat transport effects - catalyst particles. Available at: <http://www.dct.tudelft.nl/race/education/st316/chap04.pdf>. Accessed October 25, 2003.
37. Arashi N, Hishinuma Y, Narato K, Nakajima F, Kuroda H. Mass transfer to a parallel-plate catalyst. *Int Chem Eng.* 1982;22:489-494.
38. Ref. 31, pp. 773.
39. Mears DE, diagnostic criteria for heat transport limitations in fixed bed reactors. *J Catal.* 1971;20:127-131.
40. Mears DE, test for transport limitations in experimental catalytic reactors. *Ind Eng Chem Process Des Develop.* 1971;10:541-547.
41. Carberry JJ, transport phenomena in catalytic reactions. *Ind Eng Chem Res.* 1969;61:27-35.

42. Castaldi MJ, Boorse RS, Roychoudhury S, Menacherry PV, Pfefferle WC. A compact lightweight, fast-response preferential oxidation reactor for PEM automotive fuel cell applications. Proceedings of the National Science Foundation's Annual SBIR/STTR Meeting, San Juan, Puerto Rico, 2002. Available at: www.precision-combustion.com/proxpaper.pdf. Accessed September 10, 2003.
43. Sirijaruphan A, Goodwin Jr. JG, Rice RW. Investigation of the initial rapid deactivation of platinum catalysts during the selective oxidation of carbon monoxide. *J Catal.* 2004;2:288-293.
44. Nibelke RH, Campman MAJ, Hoebink JHBJ, Marin GB. Kinetic study of the CO oxidation over Pt/ γ -Al₂O₃ and Pt/Rh/CeO₂/ γ -Al₂O₃ in the presence of H₂O and CO₂. *J Catal.* 1997;171:358-373.
45. Choi Y, Stenger HG. Kinetics, simulation and insights for CO selective oxidation in fuel cell applications. *J Power Sources.* 2004;129:246-254.
46. Ouyang X, Besser RS. Effect of reactor heat transfer limitations on CO preferential oxidation. Submitted to *J Power Sources.* 2004.
46. Mergler YJ, van Aalst A, van Delft J, Nieuwenhuys BE. CO oxidation over promoted Pt catalysts. *Appl Catal, B.* 1996;10:245-261.
47. Muraki H., Matunaga SI, Shinjoh H, Wainwright MS, Trimm DL. The effect of steam and hydrogen in promoting the oxidation of carbon monoxide over a platinum on alumina catalyst. *J Chem Technol Biotechnol.* 1991;52:415-424.

NOTATION

a	depth of microchannel (m)
b	width of microchannel (m)
Bi	Biot number for heat transfer
C_{CO}	CO gas concentration (mol/m ³)
C_{O_2}	O ₂ gas concentration (mol/m ³)
C_{WP}	Weisz-Prater (W-P) parameter
d_p	catalyst heat conduction distance: catalyst thickness for the microreactor or particle diameter for the u-PBR (m)
D	catalyst dispersion
D_a	Damköhler's number for heat transport
D_e	overall mass diffusivity of O ₂ in a porous solid (m ² /s)
D_{CO}	mass diffusivity of CO in the feed mixture (m ² /s)
$D_{O_2,e}$	ordinary diffusivity of O ₂ in reformat in a porous solid (m ² /s)
D_h	hydraulic diameter of the microchannel (m)
$D_{k,e}$	Knudsen diffusivity for a porous solid (m ² /s)
E_a	Activation energy of CO oxidation in PrOx (J/mol-K)
F_{CO}	CO gas flow rate in the feed mixture (mol/s)
F_{tot}	Total reactant feed rate (Ncm ³ /min)
h	convective heat transfer coefficient of the reaction mixture (W/m ² -K)
ΔH	reaction enthalpy (J/mol)
k_{c-CO}	mass transfer coefficient of CO (m/s)
k_r	specific reaction rate (mol ^{1-α-β} /m ^{2-3(α+β)} -s)

l	reactor axial position, $l = 0$ for the entrance of the reactor
l_{Tmax}	the axial position where the temperature (at $r = 0$) is the highest
L	length of the microchannel (m)
L_c	“characteristic diffusion distance”: catalyst thickness for the microreactor (m)
m_{cat}	active metal loading of catalyst (g)
M_{Pt}	atomic weight of Pt (g/mol)
n_{CO}	molar flow rate of CO (mol/s)
n_{O_2}	molar flow rate of O ₂ (mol/s)
P_{tot}	total pressure in the reactor (atm)
P_{CO}	partial pressure of CO (atm)
P_{O_2}	partial pressure of O ₂ (atm)
v	gas velocity of the feed mixture (m/s)
r	reactor radial position, $r = 0$ for the center of the reactor
$-r_{CO}$	CO reaction rate (mol/m ³ -s)
$-r_{CO}''$	CO reaction rate (mol/m ² -s)
r_{CO_2}'	CO ₂ production rate (mol/gram of active metal of catalyst-s)
$-r_{O_2}''(obs)$	observed (actual) O ₂ reaction rate at the entrance of the microchannel (mol/m ² -s)
R	gas constant (J/mol-K)
Re	Reynolds number
S	CO ₂ selectivity
S_a	nominal surface area of the microchannel (m ²)
Sh	Sherwood number

t_{cat}	effective interparticle heat conduction distance: catalyst thickness for the microreactor or reactor inner radius for m-PBR (m)
T	reaction temperature (°C)
T_w	reactor wall temperature (°C)
TOF	turnover frequency of CO oxidation on Pt (molecules/site-s)
W_{CO}	external mass transfer rate of CO (mol/m ² -s)
$WHSV$	weight hourly space velocity, defined as moles of CO reactant flow per mole of precious metal in the catalyst per hour (hr ⁻¹)
X	reaction conversion of CO

Greek symbols

ϕ_n	Thiele modulus of n th ($n \geq 0$) order reaction
η_i	internal effectiveness factor of catalyst
ρ_c	catalyst density (g/m ³)
ρ	gas density of the feed mixture (g/m ³)
μ	gas viscosity (g/m-s)
λ	process parameter
λ_e	effective thermal conductivity of the catalyst (W/m-K)

Subscripts

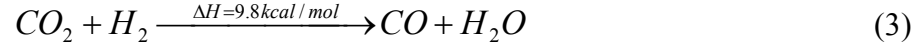
0	initial condition
s	surface condition
b	bulk condition

Superscripts

α reaction order in CO

β reaction order in O₂

EQUATIONS



$$X_{CO} = \frac{\Delta n_{CO}}{n_{CO(in)}} \quad (4)$$

$$S = \frac{0.5 \Delta n_{CO}}{\Delta n_{O_2}} \quad (5)$$

$$\lambda = \frac{2n_{O_2}}{n_{CO}} \quad (6)$$

$$C_{WP} = \eta \phi_1^2 = \frac{-r_{O_2}''(obs) \rho_c L_c^2}{D_e C_{O_2(s)}} \quad (7)$$

$$\frac{1}{D_e} = \frac{1}{D_{K,e}} + \frac{1}{D_{O_2,e}} \quad (8)$$

$$W_{CO} = k_{c-CO} (C_{CO(b)} - C_{CO(s)}) \quad (9)$$

$$Sh = 6.0 + 0.0006 \left(\frac{Re}{L/2b} \right)^{1.36} \quad (10)$$

$$Sh = \frac{8k_c b}{D_{CO}} \quad (11)$$

$$Re = \frac{\rho v D_h}{\mu} \quad (12)$$

$$D_h = \frac{2ab}{a+b} \quad (13)$$

$$-r_{CO}'' = F_{CO(0)} \frac{dX}{dS_a} \cong F_{CO(0)} \frac{X}{S_a} \quad (14)$$

$$-r_{CO}'' = k_r C_{CO}^\alpha C_{O_2}^\beta = k_r C_{CO(0)}^{\alpha+\beta} (1-X)^\alpha \left(\frac{C_{O_2(0)}}{C_{CO(0)}} - 0.5X \right)^\beta \quad (15)$$

$$D_a = \frac{|\Delta H(-r_{CO})t_{cat}^2|}{\lambda_e T_w} < 0.4 \frac{RT_w}{E_a} \quad (16)$$

$$Bi = \frac{hd_p}{\lambda_e} < 10 \quad (17)$$

$$TOF = \frac{r_{CO_2}' \times M_{Pt}}{D \times m_{cat}} \quad (18)$$

No.	Reaction	A*	E _a *	k ₃₇₃	k ₄₅₃	k ₅₇₃
1	H ₂ + 2Pt(s) → 2H(s)	4.60E-02	0	4.60E-02	4.60E-02	4.60E-02
2	O ₂ + 2Pt(s) → 2O(s)	2.00E-05	-25	6.37E-02	1.53E-02	3.81E-03
3	CO + Pt(s) → CO(s)	8.40E-01	0	8.40E-01	8.40E-01	8.40E-01
4	CO ₂ + Pt(s) → CO ₂ (s)	5.00E-03	0	5.00E-03	5.00E-03	5.00E-03
5	H ₂ O + Pt(s) → H ₂ O(s)	7.50E-01	0	7.50E-01	7.50E-01	7.50E-01
6	H + Pt(s) → H(s)	1	0	1.00E+00	1.00E+00	1.00E+00
7	O + Pt(s) → O(s)	1	0	1.00E+00	1.00E+00	1.00E+00
8	OH + Pt(s) → OH(s)	1	0	1.00E+00	1.00E+00	1.00E+00
9 ^a	2H(s) → 2Pt(s) + H ₂	3.70E+21	67.4-10.0θ _H	1.61E+12	8.83E+13	4.42E+15
10 ^a	2O(s) → O ₂ + 2Pt(s)	3.70E+21	227.4-188.3θ _O	5.09E-11	2.16E-05	6.73E+00
11 ^a	CO(s) → CO + Pt(s)	2.00E+16	146-33.0θ _{CO}	1.58E+00	5.68E+02	1.24E+05
12	CO ₂ (s) → CO ₂ + Pt(s)	1.00E+13	27.1	1.60E+09	7.47E+09	3.38E+10
13	H ₂ O(s) → H ₂ O + Pt(s)	4.50E+12	41.8	6.26E+06	6.77E+07	6.93E+08
14 ^a	H(s) → H + Pt(s)	6.00E+13	254.4-5.0θ _H	1.50E-22	3.20E-16	4.87E-10
15 ^a	O(s) → O + Pt(s)	1.00E+13	358.8-94.1θ _O	5.34E-38	4.04E-29	1.88E-20
16 ^a	OH(s) → OH + Pt(s)	5.00E+13	251.1-167.4θ _O	3.29E-22	5.37E-16	6.26E-10
17 ^a	CO(s) + O(s) → CO ₂ (s) + Pt(s)	3.70E+19	117.6-33.0θ _{CO}	2.78E+07	1.99E+09	8.94E+10
18 ^a	CO ₂ (s) + Pt(s) → CO(s) + O(s)	3.70E+19	173.3+94.1θ _O	1.94E-05	3.76E-01	5.78E+03
19	C(s) + O(s) → CO(s) + Pt(s)	3.70E+19	0	3.70E+19	3.70E+19	3.70E+19
20 ^a	CO(s) + Pt(s) → C(s) + O(s)	3.70E+19	236.5-33.0θ _{CO}	6.09E-10	3.81E-05	1.28E+00
21 ^a	CO(s) + OH(s) → CO ₂ (s) + H(s)	2.00E+19	38.7-33.0θ _{CO}	1.70E+18	1.36E+18	7.59E+17
22	CO ₂ (s) + H(s) → CO(s) + OH(s)	2.00E+19	28.3	2.17E+15	1.09E+16	5.25E+16
23	H(s) + O(s) → OH(s) + Pt(s)	1.30E+21	11.2	3.51E+19	6.63E+19	1.24E+20
24 ^a	OH(s) + Pt(s) → H(s) + O(s)	7.39E+19	77.3-73.2θ _O	1.09E+09	8.93E+10	6.58E+12
25	H(s) + OH(s) → H ₂ O(s) + Pt(s)	2.04E+21	66.22	1.08E+12	4.68E+13	1.86E+15
26 ^a	H ₂ O(s) + Pt(s) → H(s) + OH(s)	1.15E+19	101.4+167.4θ _O	7.13E+04	2.30E+07	6.49E+09
27	2OH(s) → H ₂ O(s) + O(s)	7.40E+20	74	3.17E+10	2.15E+12	1.32E+14
28 ^a	H ₂ O(s) + O(s) → 2OH(s)	1.00E+20	43.1+240.6θ _O	9.15E+13	1.07E+15	1.17E+16

Table 1. Elementary surface reactions used in the microkinetic reaction modeling [26,27]. k_{T_y} (rate constant for elementary reaction at temperature T_y for the reactor entrance) = $A_x \cdot \exp(-E_{a_x}/RT)$. E_{a_x} : kJ/mol, R : 0.00831 kJ/(mol·K), θ_x : mole fraction of surface species x . ^aThe activation energy for the reaction depends on the mole fraction of the species surface species.

References	Catalyst System	Temperature (°C)	Pressure (atm)	P _{CO} (Torr)	P _{O₂} (Torr)	P _{H₂} (Torr)	λ	TOF (s ⁻¹)
This work	Pt/γ-Al ₂ O ₃ (D=20%)	100°C	1	13.68	13.68	469.68	2	0.006
Sirijaruphan, et al. [42]	Pt/γ-Al ₂ O ₃ (D=45.4%)	90°C	1.8	13.68	13.68	342.00	2	0.009
This work	Pt/γ-Al ₂ O ₃ (D=20%)	150°C	1	7.60	7.60	469.68	2	0.077
This work	Pt/γ-Al ₂ O ₃ (D=20%)	150°C	1	15.20	15.20	0.00	2	0.020
This work	Pt/γ-Al ₂ O ₃ (D=20%)	150°C	1	7.60	3.30	0.00	0.87	0.009
Kahlich, et al. [3]	Pt/γ-Al ₂ O ₃ (D=38%)	150°C	1	7.60	7.60	570.00	2	0.080
Mergler, et al. [46]	Pt/γ-Al ₂ O ₃ (D=68%)	150°C	1	15.20	15.20	0.00	2	0.004
Muraki et al. [47]	Pt/γ-Al ₂ O ₃ (D=22%)	150°C	1	7.60	3.30	0.00	0.87	0.011
This work	Pt/γ-Al ₂ O ₃ (D=20%)	200°C	1	7.60	7.60	469.68	2	1.266
This work	Pt/γ-Al ₂ O ₃ (D=20%)	200°C	1	7.60	7.60	0.00	2	0.452
Kahlich, et al. [3]	Pt/γ-Al ₂ O ₃ (D=38%)	200°C	1	7.60	7.60	570.00	2	0.710
Kim, et al. [15]	Pt/γ-Al ₂ O ₃ (D=100%)	200°C	1	7.60	7.60	380.00	2	0.330
Nibbelke, et al. [40]	Pt/γ-Al ₂ O ₃	210°C	1	7.60	7.60	0.00	2	0.625
This work	Pt/γ-Al ₂ O ₃ (D=20%)	220°C	1	10.00	10.00	0.00	2	0.584
Ajmera, et al. [16]	Pt/γ-Al ₂ O ₃	230°C	1.5	11.40	11.40	0.00	2	0.780
This work	Pt/γ-Al ₂ O ₃ (D=10%)	250°C	1	7.60	7.60	469.68	2	4.831
This work	Pt/γ-Al ₂ O ₃ (D=20%)	250°C	1	10.00	10.00	0.00	2	1.932
Kahlich, et al. [3]	Pt/γ-Al ₂ O ₃ (D=38%)	250°C	1	7.60	7.60	570.00	2	3.800
Zafiris, et al. [4]	Pt/α-Al ₂ O ₃ (0001)	250°C	1	10.00	10.00	0.00	2	0.500

Table 2. Comparison of different Pt/Al₂O₃ catalyst system for PrOx with *TOF* calculations for 5 temperature regions (~100°C, 150°C, ~200°C, ~220°C, 250°C). D – catalyst dispersion.

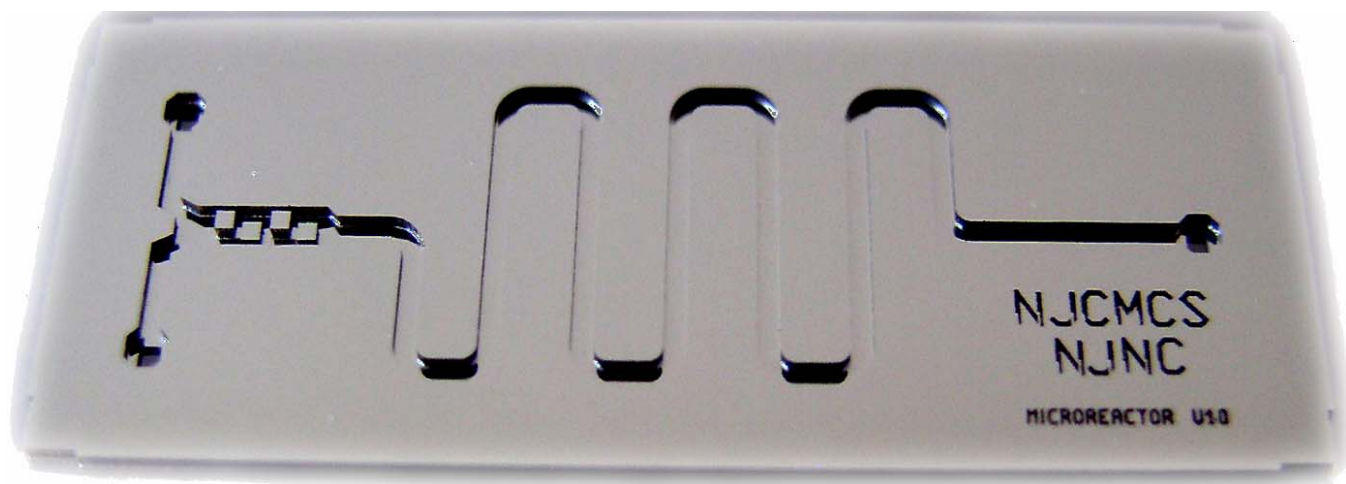


Figure 1. A Si microreactor used in this research, with two inlets, a pre-mixer, a catalyzed reaction zone and an outlet cooling zone for reaction quenching. Channel Dimensions: 500 μm (W) x 610 μm (D) x 4.5 cm (L).

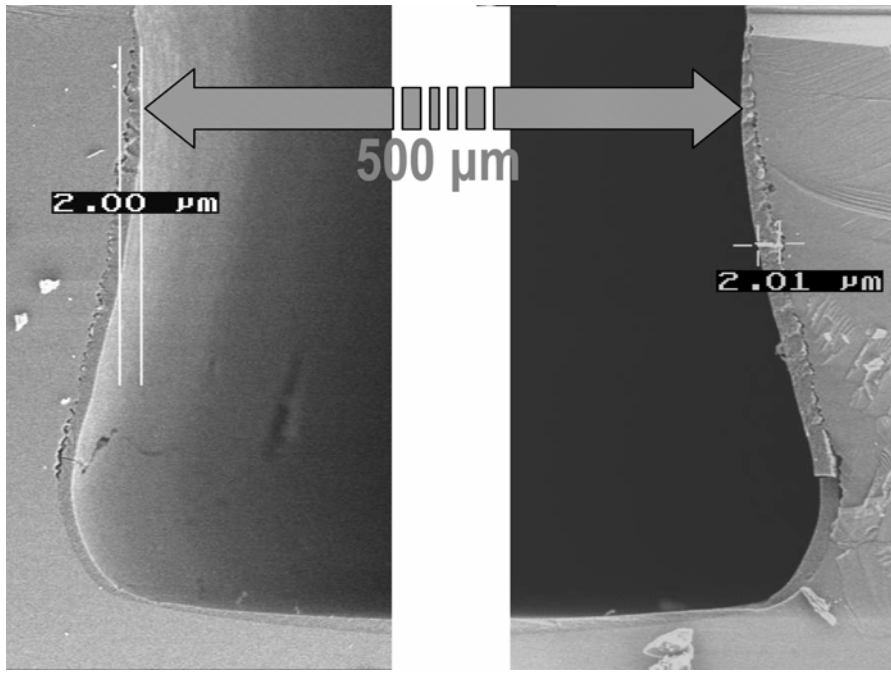


Figure 2. SEM photo of cross-section of the microchannel with thin-film coating.

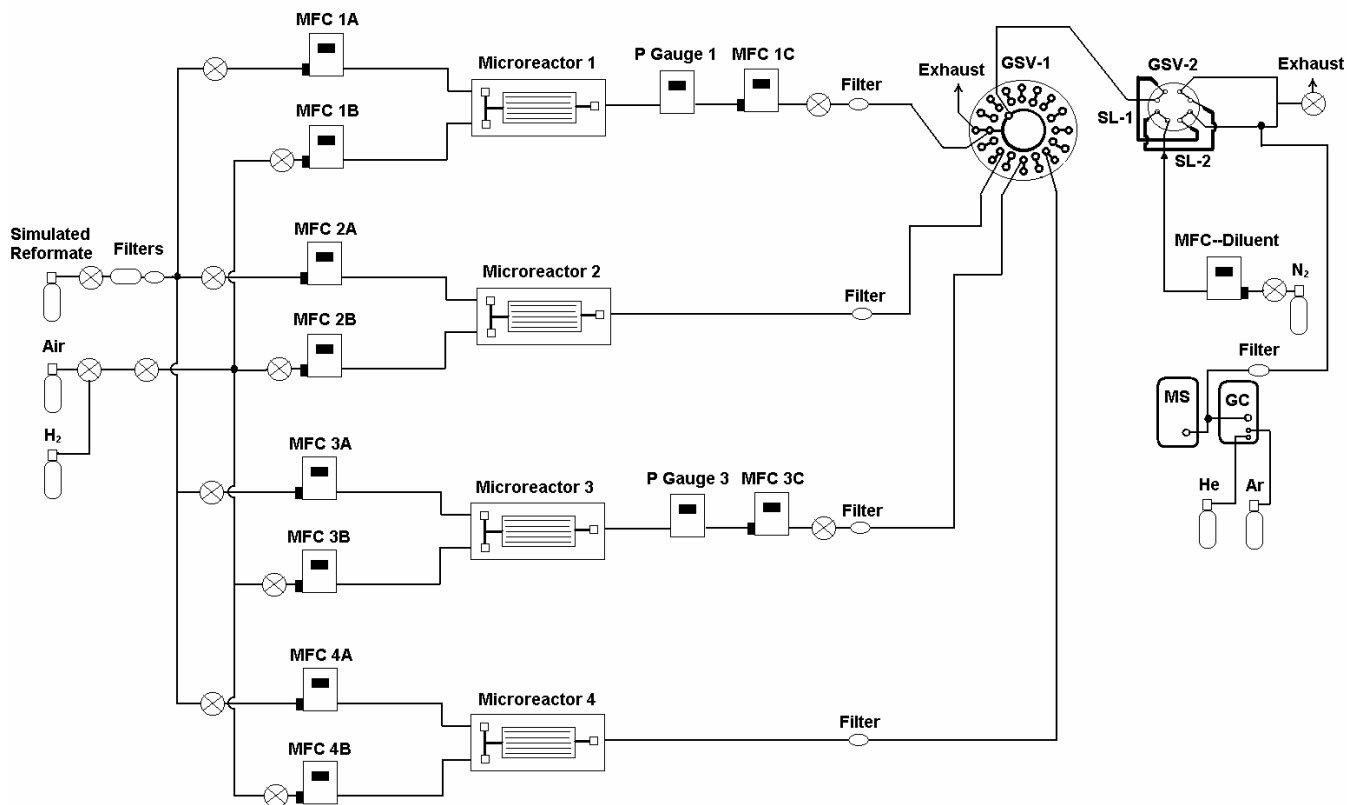


Figure 3. Microkinetic array for multiple catalyst screening and process optimization: 4 reactors are screened in a multiplex fashion implemented by two gas sampling valves.

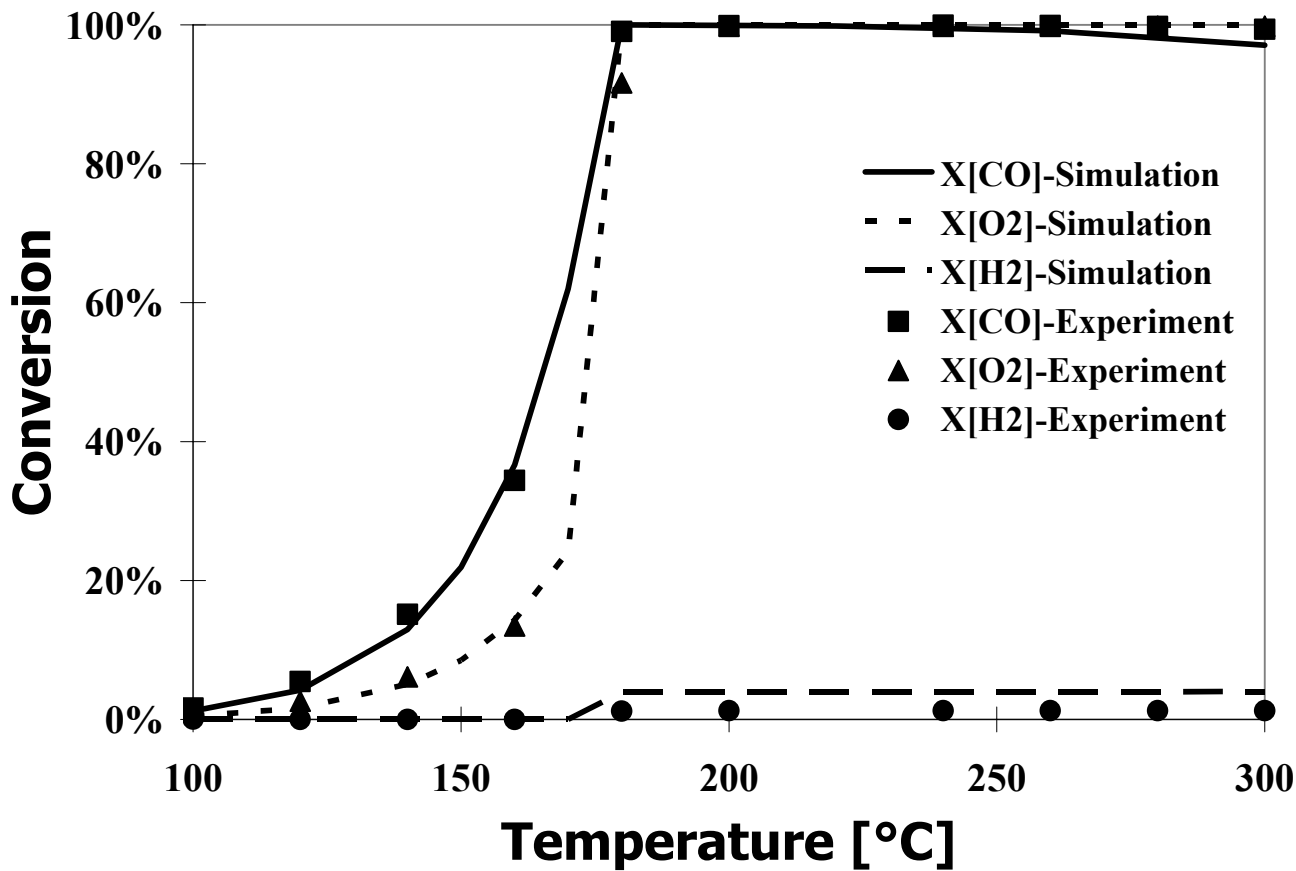


Figure 4. CHEMKIN[®] simulation agreed well with experimental results for X_{CO} , X_{O_2} and X_{H_2} . $WHSV = 1500 \text{ hr}^{-1}$, $F(\text{mixture 1}) = 5.0 \text{ Ncm}^3/\text{min}$, $F(\text{air}) = 0.5 \text{ Ncm}^3/\text{min}$.

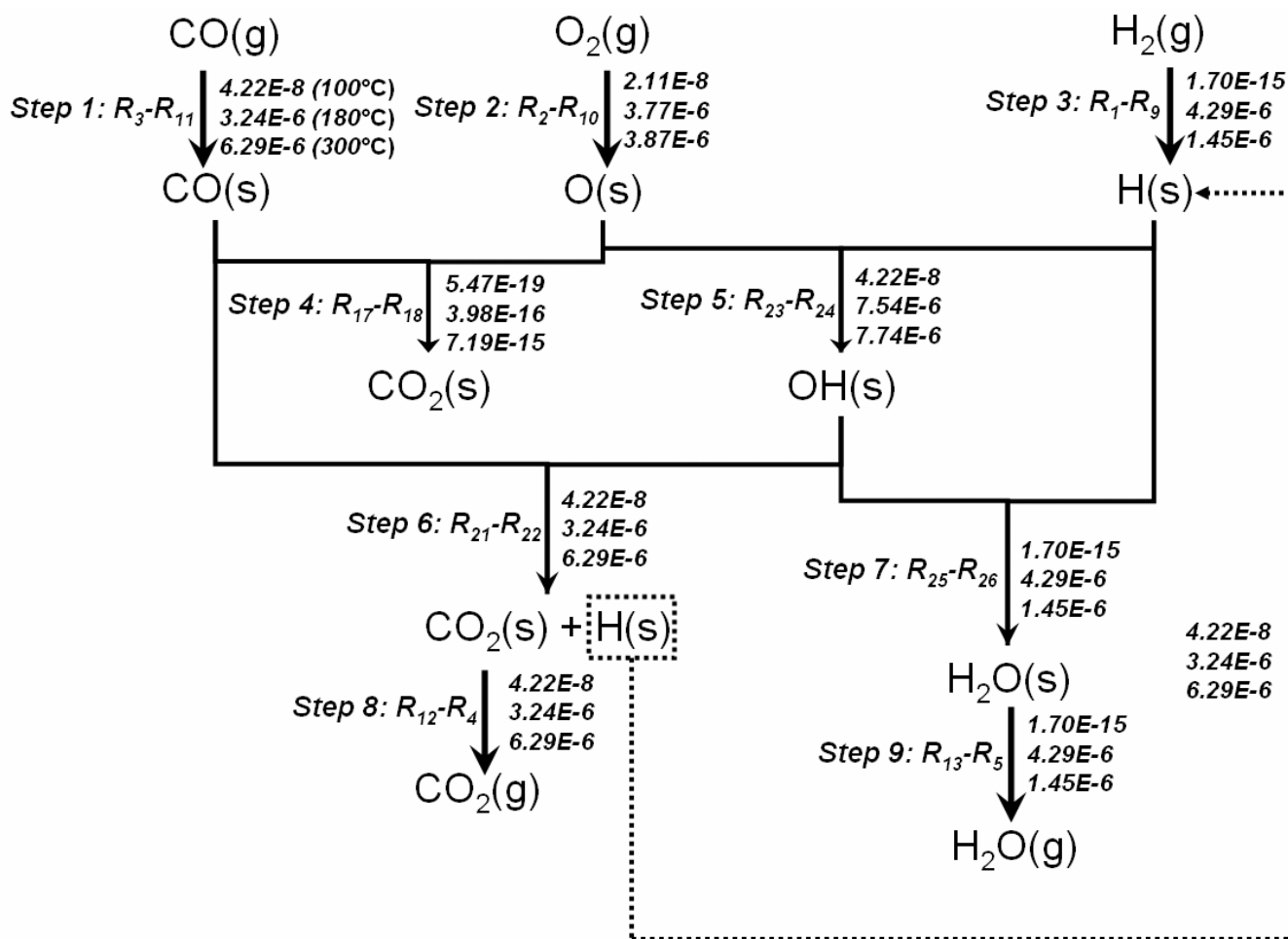


Figure 5. Elementary reaction network shows the pathways involving CO₂, H₂O and CO. Steady-state reaction rates (mol/s) in the whole microreactor at 100°C, 180°C and 300°C are also shown. WHSV = 1500 hr⁻¹, F(mixture 1) = 5.0 Ncm³/min, F(air) = 0.5 Ncm³/min.

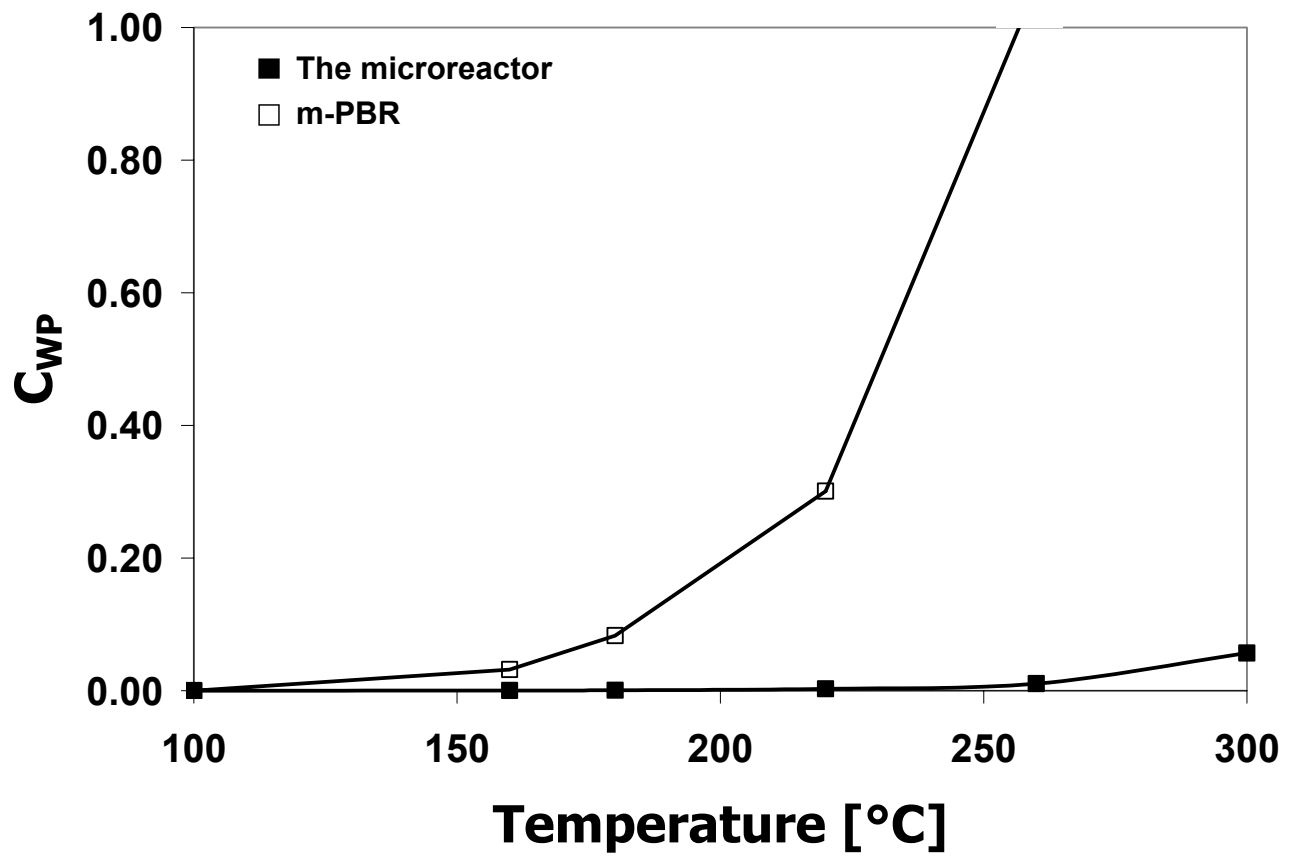


Figure 6. The Weisz-Prater parameters for both the microreactor and the m-PBR at different temperatures.

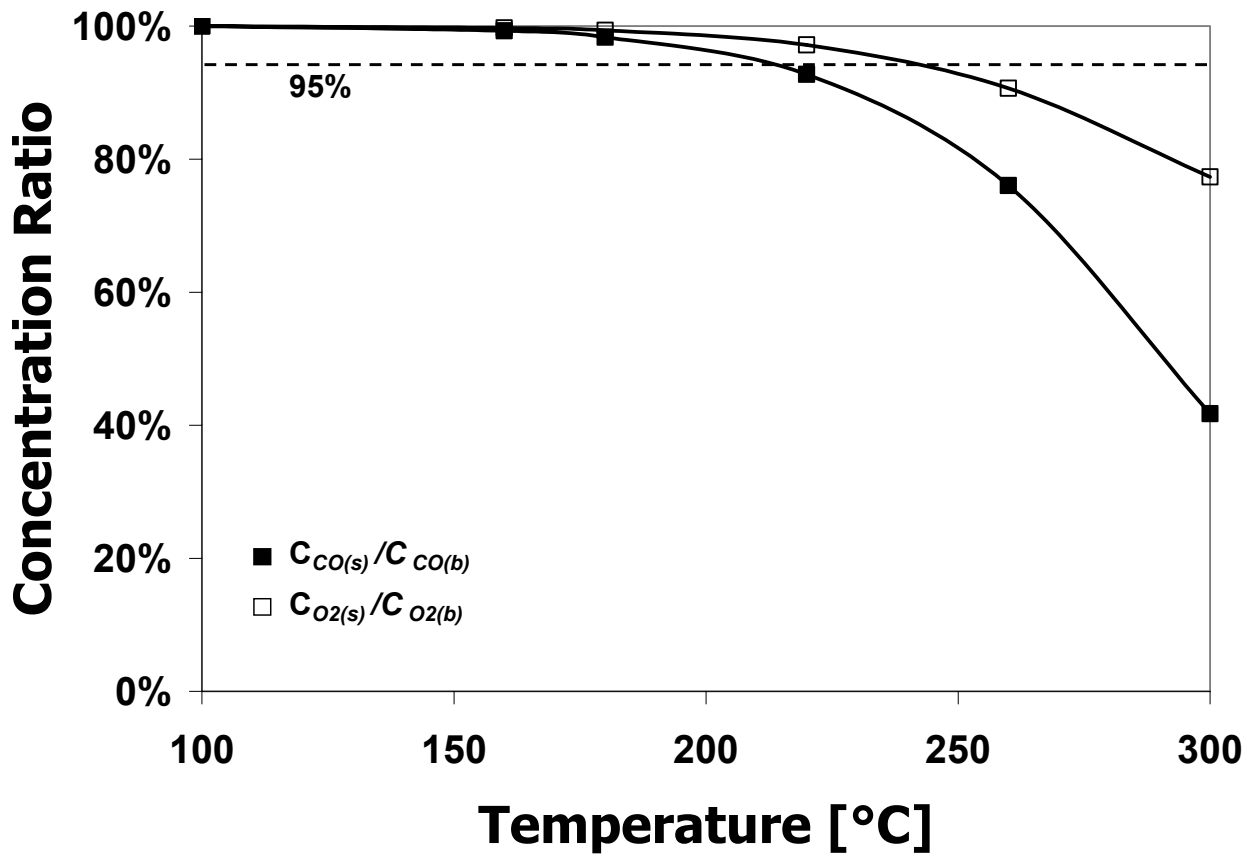


Figure 7. Calculated ratios of $C_{CO(s)}/C_{CO(b)}$ and $C_{O_2(s)}/C_{O_2(b)}$ from mass-transport analysis at different temperatures in differential flow conditions for the microreactor.

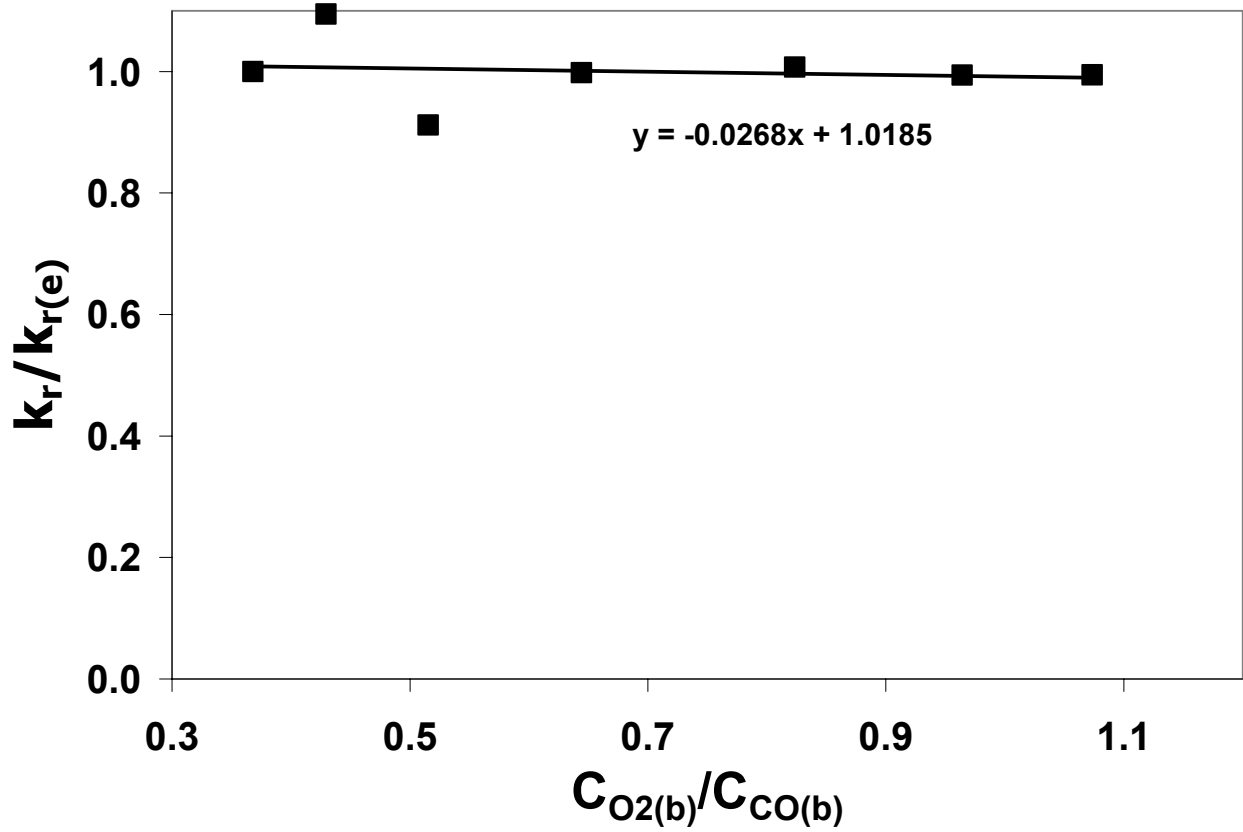


Figure 8. Ratios of experimental specific reaction rate (k_r) and average specific reaction rate ($k_{r(e)}$) for different $C_{O_2(b)}/C_{CO(b)}$ ratios show that external mass transport limitations are not important at 180°C.

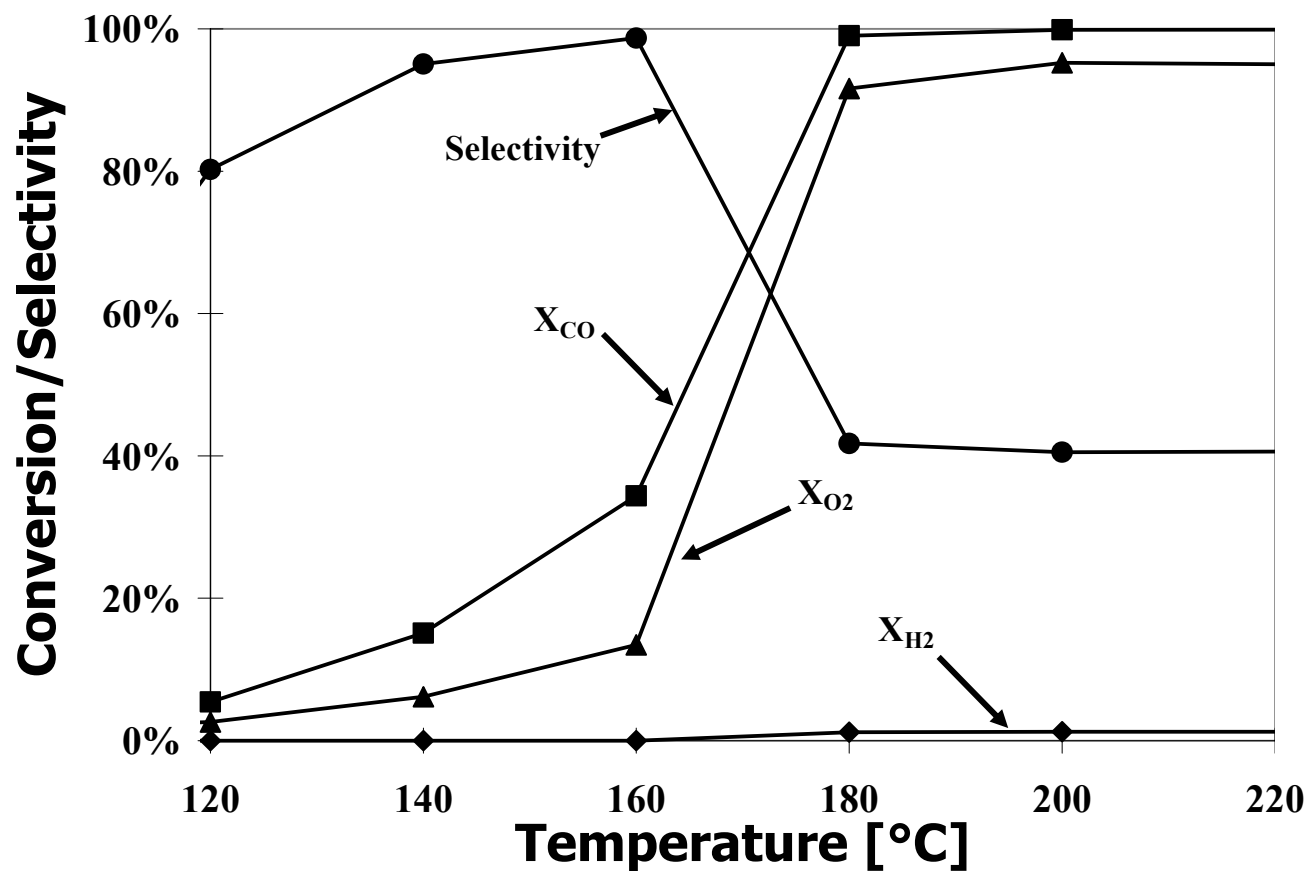


Figure 9. Experimental conversion of CO, O₂, H₂ and selectivity of CO₂ at different temperatures in the microreactor. WHSV = 1500 hr⁻¹, F(mixture 1) = 5.0 Ncm³/min, F(air) = 0.5 Ncm³/min.

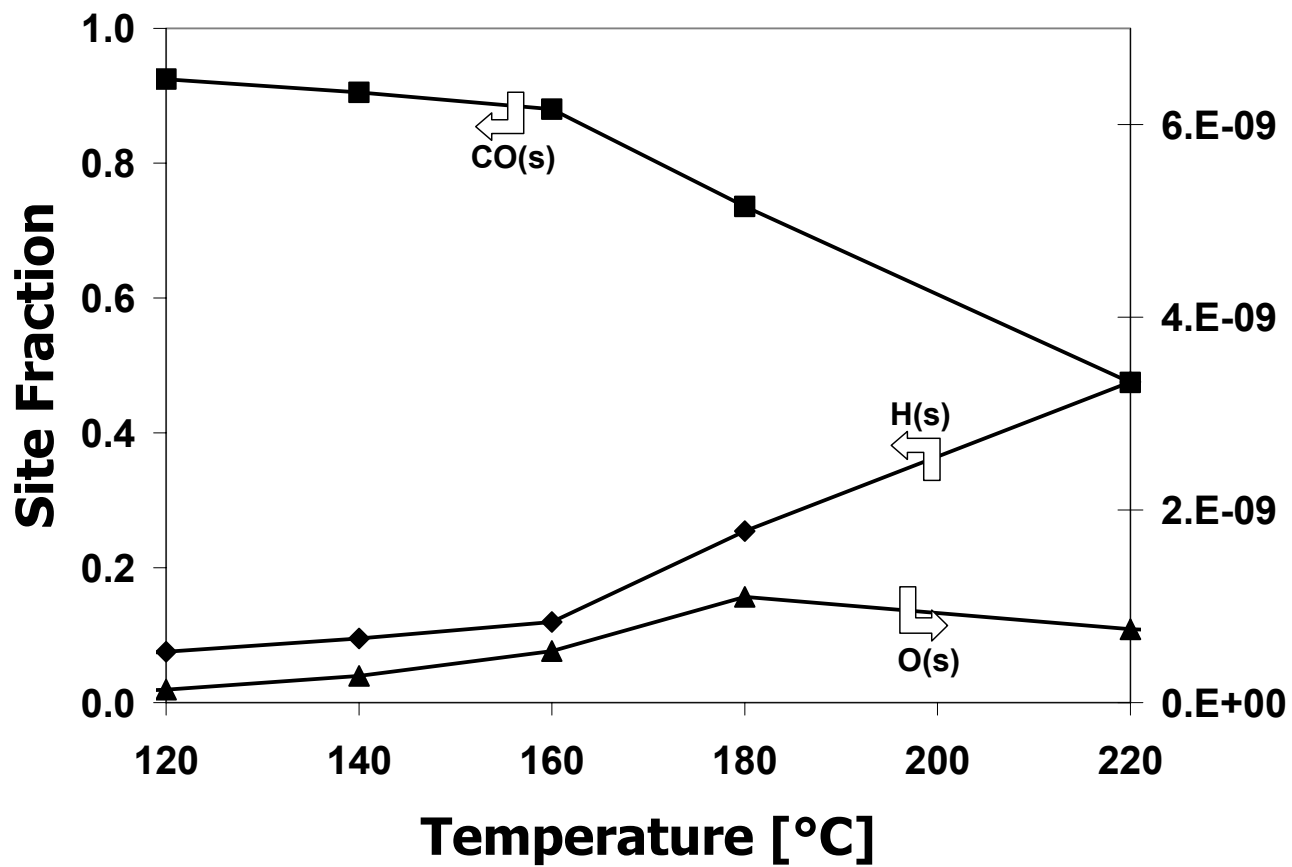


Figure 10. Microkinetic simulations show that CO(s), H(s) and O(s) site fractions vary with temperature. WHSV = 1500 hr⁻¹, F(mixture 1) = 5.0 Ncm³/min, F(air) = 0.5 Ncm³/min.

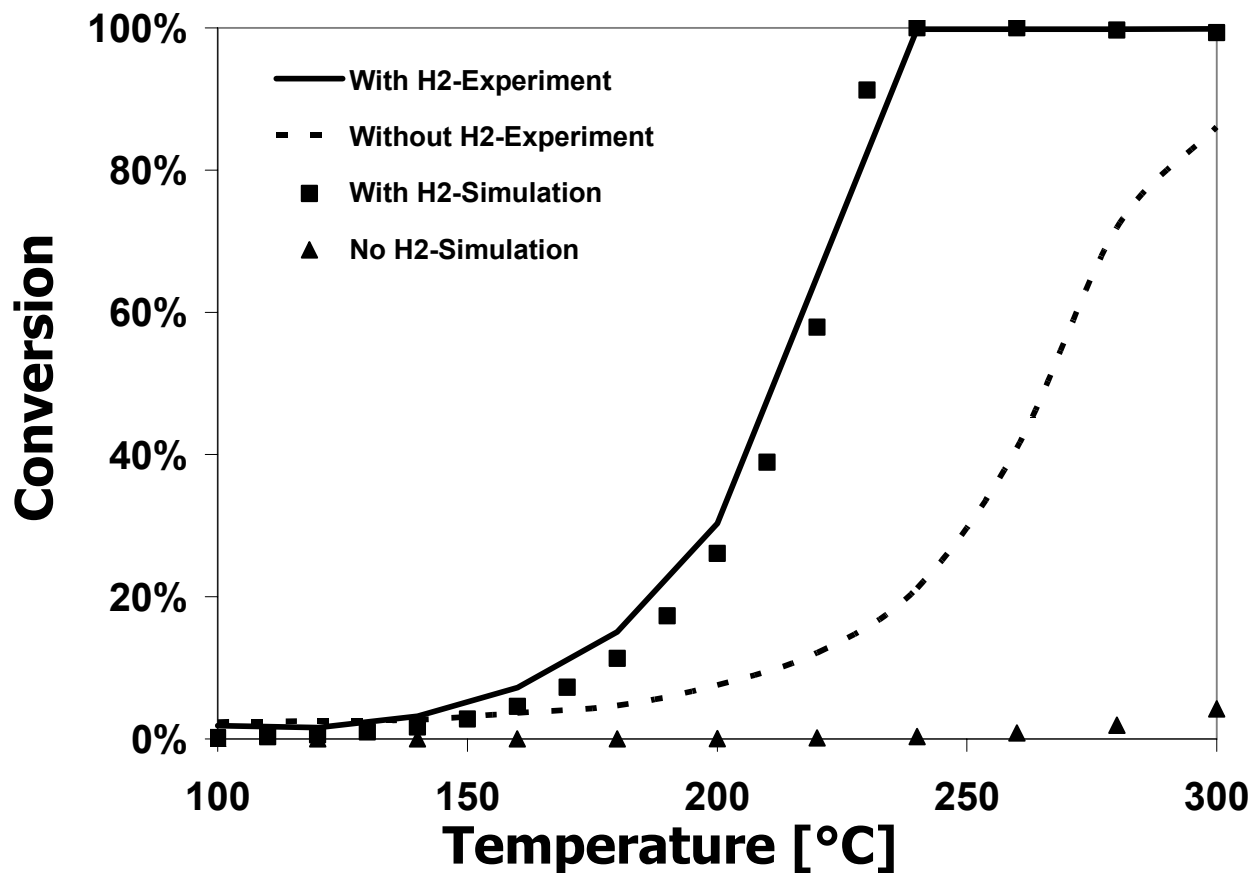


Figure 11. Experimental and simulation results indicate that the addition of H₂ significantly increases CO conversion. WHSV = 11000 hr⁻¹, F(mixture 1 or 2) = 5.0 Ncm³/min, F(air) = 0.5 Ncm³/min.

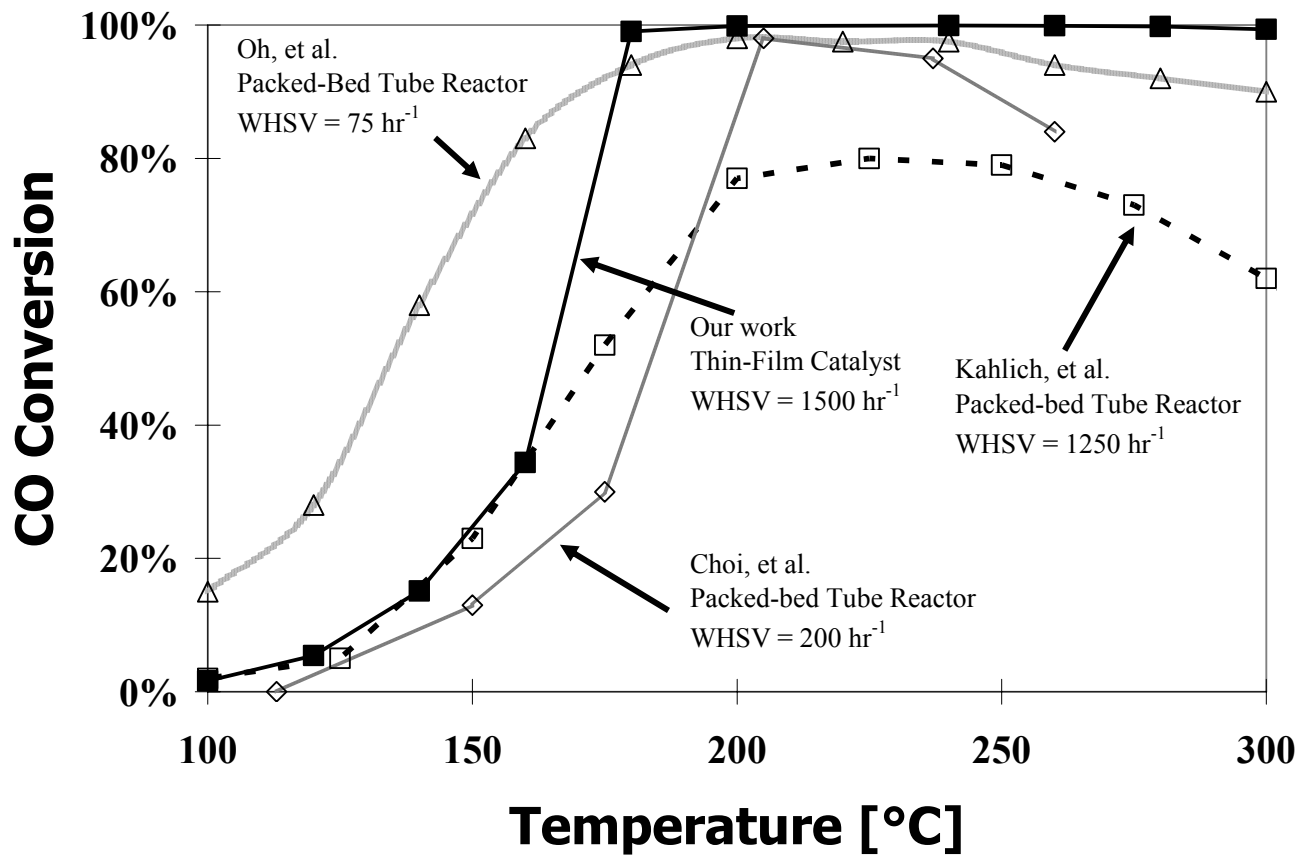


Figure 12. CO conversion vs. temperature: comparison of the results of microreactor to those of other PrOx studies in the literature. WHSV: our work – 1500 hr⁻¹, Kahlich et al. [3] – 1250 hr⁻¹, Oh et al. [8] – 75 hr⁻¹, Choi et al. [44] – 200 hr⁻¹. λ : our work – 2.57, all other three – 2.0.

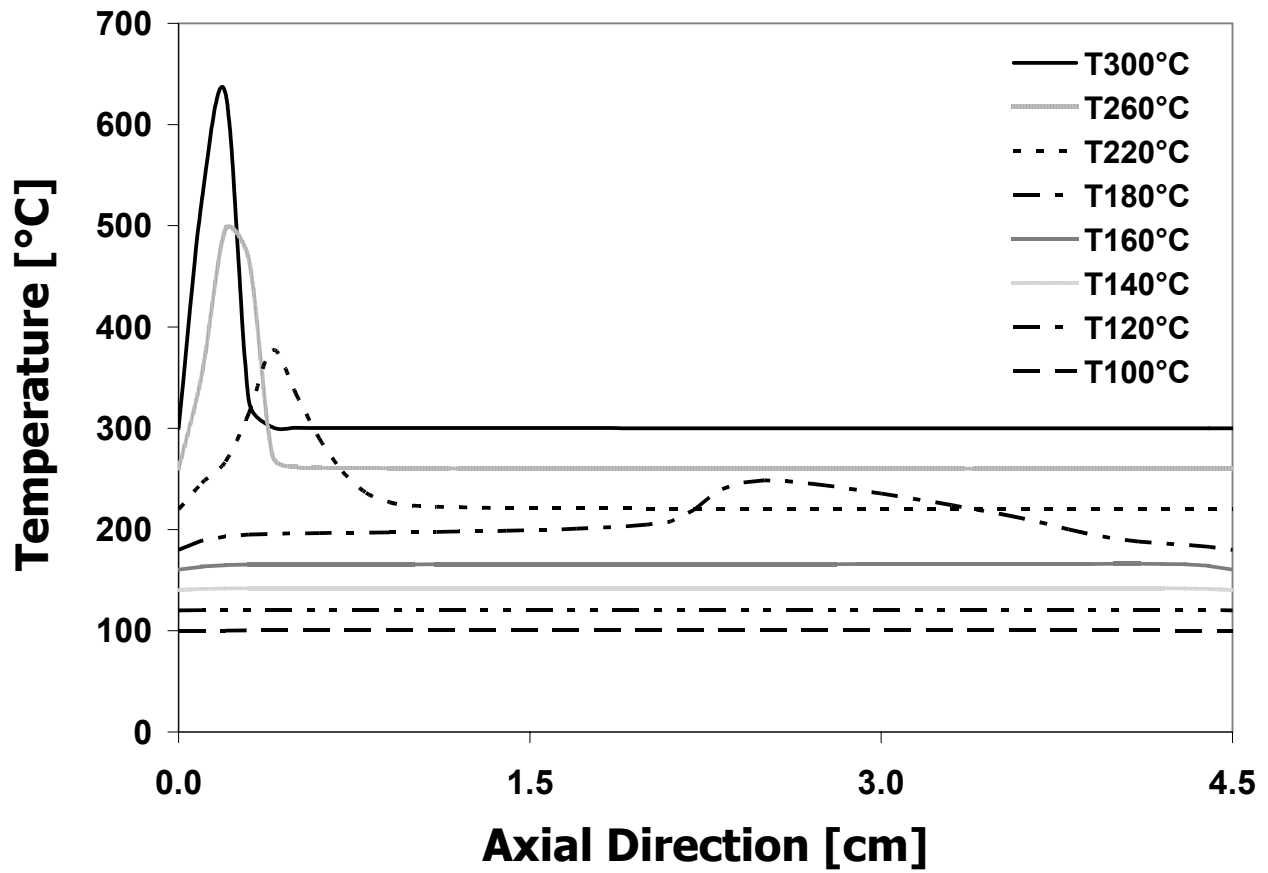


Figure 13. Calculated temperature distribution in the axial direction at $r = 0.2$ mm for the 2-mm m-PBR. WHSV: 1500 hr^{-1} .

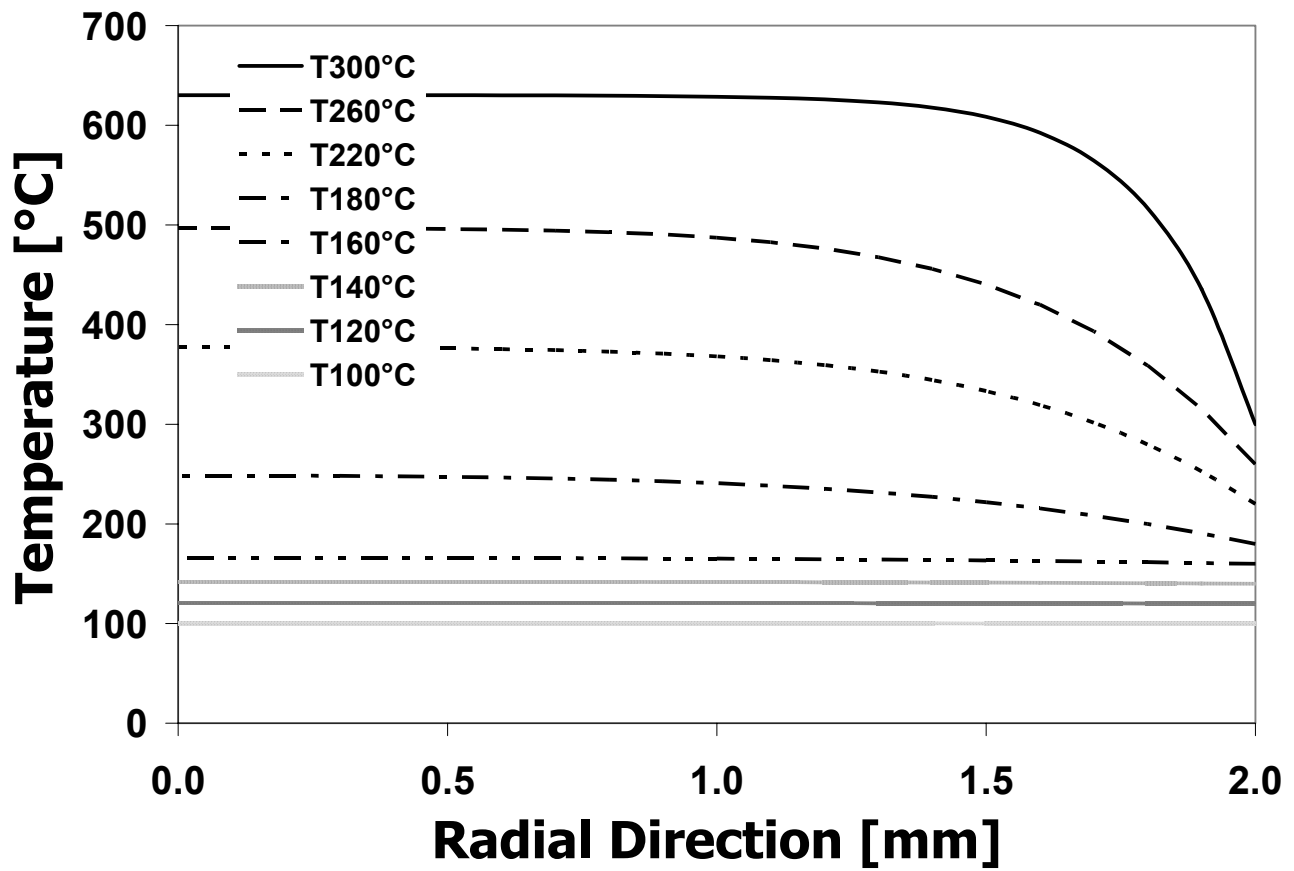


Figure 14. Calculated temperature distribution in the radial direction at $l = l_{T_{max}}$ for the 2-mm m-PBR. WHSV: 1500 hr^{-1} .

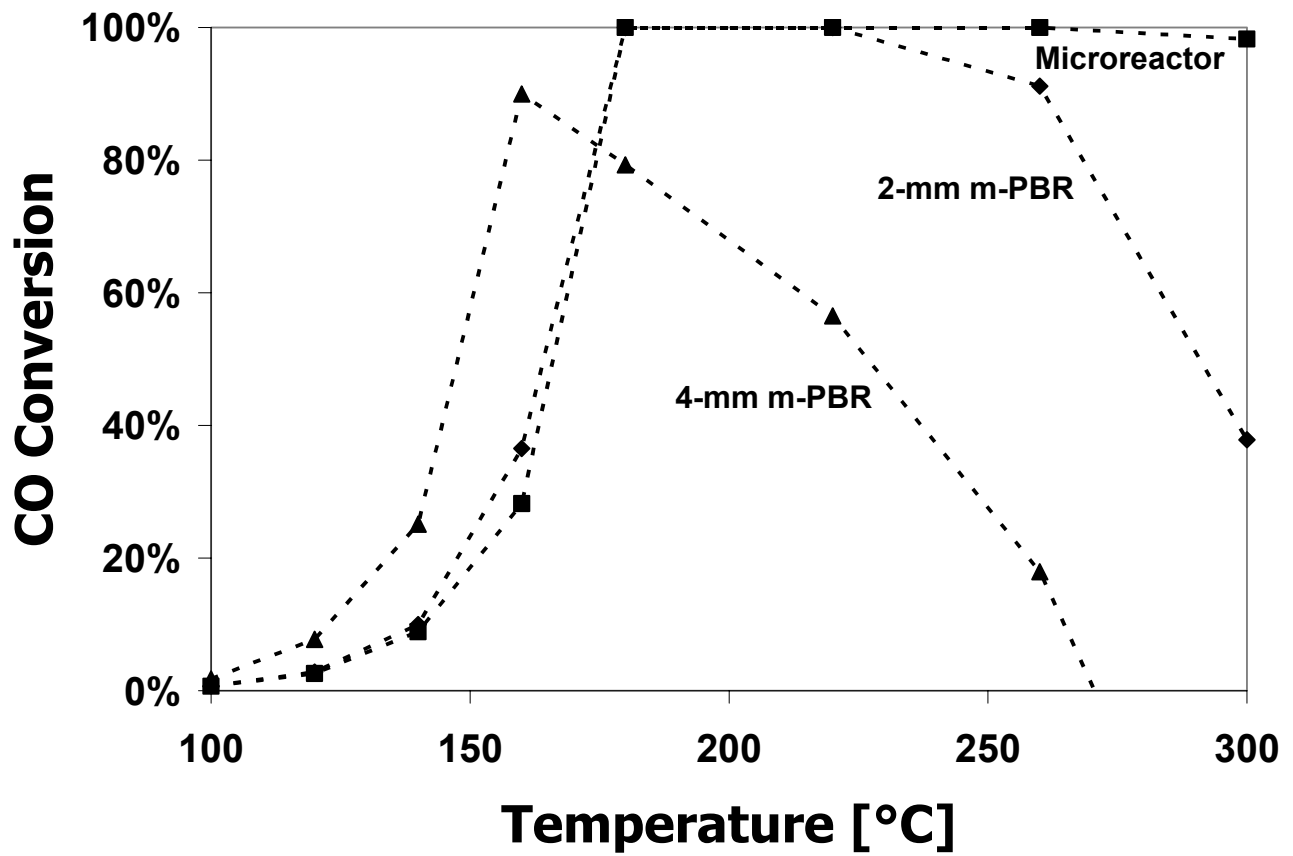


Figure 15. Calculated CO conversion vs. different reactor wall temperatures for the microreactor, 2-mm and 4-mm m-PBR's. WHSV: 1500 hr⁻¹.

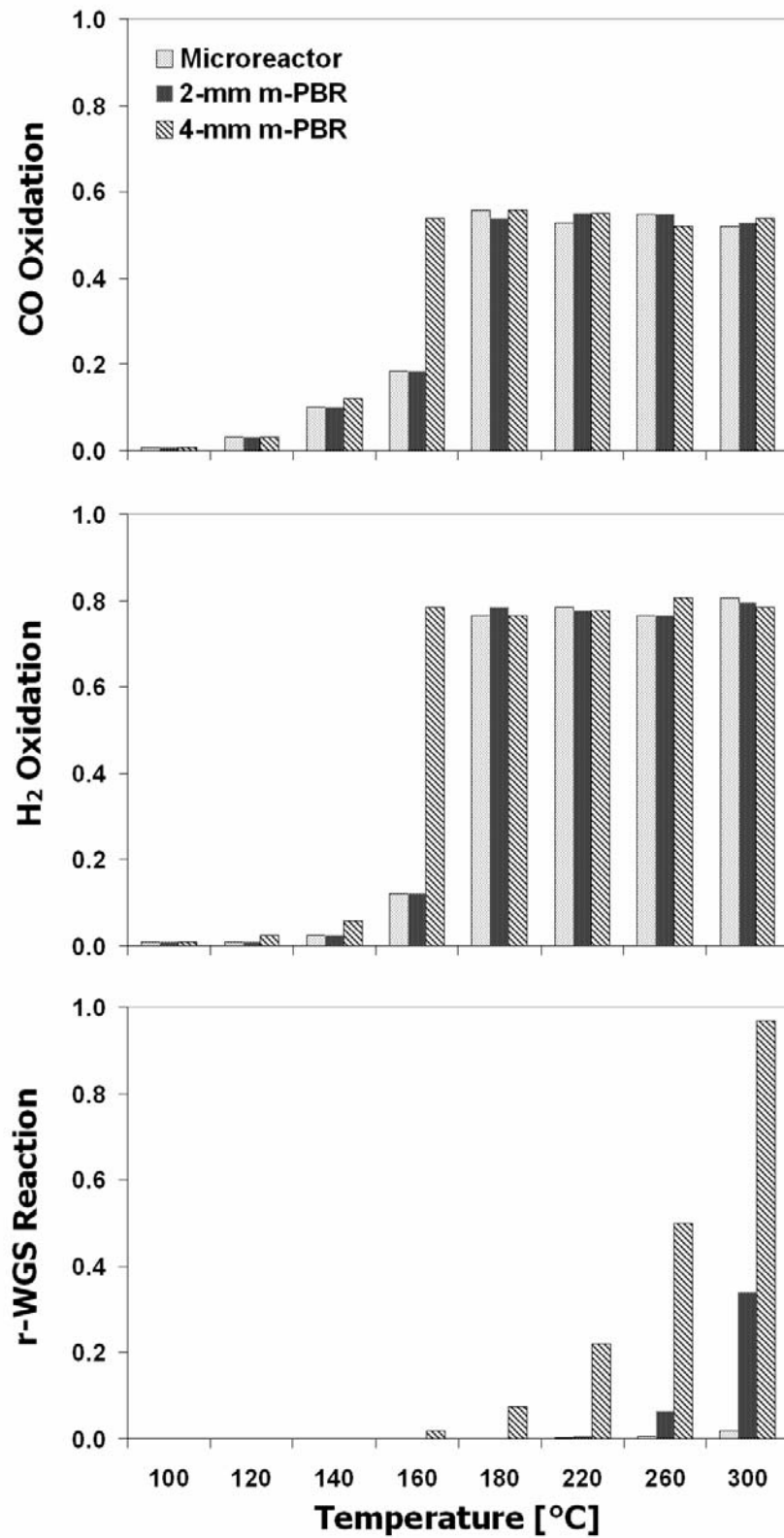


Figure 16. The reaction rates for CO oxidation, H₂ oxidation and the r-WGS reaction at different temperatures for the microreactor, 2-mm and 4-mm m-PBR's. WHSV = 1500 hr⁻¹.